Fine-tuning of ^{210}Pb-based methods for dating vegetated saltmarsh sediments

A.R. Iurian [a,c], G. Millward [b], W. Blake [b,c], J.M. Abril Hernández [d,*]

[a] Terrestrial Environment Laboratory, IAEA Environment Laboratories, Department of Nuclear Sciences and Applications, International Atomic Energy Agency, Vienna International Centre, PO Box 100, Vienna, 1400, Austria

[b] Consolidated Radioisotope Facility (CoRiF), University of Plymouth, UK

[c] School of Geography, Earth and Environmental Sciences, University of Plymouth, Plymouth, PL4 8AA, United Kingdom

[d] Departamento de Física Aplicada I, ETSIA Universidad de Sevilla, Carretera de Utrera km 1, Seville, D.P. 41013, Spain

A B S T R A C T

Saltmarshes, wetlands, inter-tidal mudflats are highly productive natural ecosystems with significant ecological value. ^{210}Pb and ^{137}Cs have been used for establishing chronologies at a centennial scale in these sediments. They are relevant for assessing how saltmarshes are vulnerable to climate change, natural hazards and contamination from human inputs. This paper aims to review and adapt existing methods for the ^{210}Pb-based radiometric dating of these sediments where the subterranean production and decay of OM are sources of achronicity. This limits the use of the basic assumption of considering the sediment as a continuous medium. From the available evidence, ^{210}Pb fluxes onto sediments may be mediated by the activities bound to the mass flows, suggesting that models assuming a constant flux should be handled with care. The activity concentrations of excess ^{210}Pb required by CF- CS, CIC and TERESA radiometric models must be those of the sediment mineral fraction, while CRS and PLUM can work with the composite sediment matrix. A review of these issues and application of the models is illus-trated with new data from two recent saltmarsh sediment cores. The effects of non-ideal boundary conditions in radiometric dating and the system time-average of ^{137}Cs fluxes are discussed. Although specific to vegetated saltmarshes, this topic and the present results have generic applications for other vegetated coastal sediments.

Keywords:

^{210}Pb radiometric dating
Saltmarsh sediment
Mineral sediment fraction
Accretion rate
Organic matter

1. Introduction

Saltmarshes are vegetated coastal wetlands of great ecological value being commonly characterized by accreting mudflats stabilized by spreading salt tolerant (halophytic) vegetation (Allen and Pye, 1992). They are of wide interest, including paleoecology inferring sea level changes (Barnett et al., 2017), carbon storage (Livesley and Andrusiak, 2012), marsh restoration and land reclamation (Bakker et al., 2002), anthropogenic impacts and environmental forcing (Kirwan and Megonigal, 2013), marsh contaminant storage and water quality (Cundy and Croudace, 2017), and responses to changing environmental controls and sea level change (Kolker et al., 2009).

Establishing accurate dates and accretion rates in saltmarsh ecosystems is important, among other environmental studies, for i) the quantification of their carbon sequestration capacity (Kristensen et al., 2008; Nellemann et al., 2009; Marchand, 2017); ii) assessing how the acceleration in sea-level-rise linked to global warming could surpass the accretion capacity of vegetated saltmarsh sediments, resulting in an overall degradation of these habitats (Kennish, 2001; Hughes, 2004; Crosby et al., 2016); iii) decoding past anthropogenic impacts and environmental forcing (Kirwan and Megonigal, 2013).

Estimation of sedimentation rates at a centennial scale have been reported using the ^{210}Pb-based radiometric dating method (Cundy and Croudace, 1995; Wilson et al., 2014; Yang et al., 2014; Ruíz-Fernández et al., 2018). The ^{210}Pb-based ages may be supported by independent chronostratigraphic markers provided by the ^{137}Cs specific activity versus depth profile, or other radionuclides such as ^{241}Am and ^{207}Bi (Kim et al., 1997; Pedersen et al., 2007; Bellucci et al., 2007;

Abbreviations: SWI, sediment-water interface; NID, non-ideal deposition; ECL, early compaction limit; SAR, sediment accretion rates; *CR*, concentration ratio; OM, organic matter; STA, System-Time-Average; CRS, Constant Rate of Supply; CF–CS, Constant Flux-Constant Sedimentation; CIC, Constant Initial Concentration; TERESA, Time Estimates from Random Entries of Sediments and Activities.

* Corresponding author.
E-mail address: jmabril@us.es (J.M. Abril Hernández).

García-Artola et al., 2016).

In some cases, the agreement between the ^{210}Pb and ^{137}Cs derived ages is poor, or they are incompatible (Madsen et al., 2007; Marshall et al., 2007; García-Artola et al., 2016). Difficulties may arise, at least partially, from the application of radiometric dating methods originally developed for lacustrine (Krishnaswamy et al., 1971) and marine (Koide et al., 1972) sediments, without any tuning for the specific conditions pertaining in vegetated coastal sediments or without proper consideration for the specific assumptions underlying the models.

Arias-Ortiz et al. (2018) presented a comprehensive review of ^{210}Pb-based dating models for recent sediments with focus on vegetated coastal ecosystems. The paper considers and tries to numerically simulate a series of factors (namely mixing, acceleration in mass accumulation rates, erosion, grain size and organic matter decay) which can alter the shape of ideal ^{210}Pb profiles and then lead to misestimating ages, sediment accretion and carbon accumulation rates in the routinely application of CF-CS and CRS models.

Annex A presents a brief description of the ^{210}Pb dating method and reviews the assumptions adopted by a series of models excluding post-depositional redistribution, namely the models CRS (constant rate of supply), CIC (constant initial concentration), CF-CS (constant flux with constant sedimentation), SIT (sediment isotope tomography), TERESA (time estimates from random entries of sediments and activities), CS (constant sedimentation rate), PLUM (the Bayesian formulation of the constant-flux model), *serac* (a R-software package including some of the previous models) and STA (system-time-average, for pre-depositional processes affecting man-made radionuclides). Discussions on the limitations in their use arising from a partial or null accomplishment of the involved assumptions related to fluxes of matter onto the sediment and radionuclides behaviour are included in Annex A. Corrections in dating models due to grain-size effects are also considered.

All models and the diagenetic equations (Abril, 2003) share the fundamental assumption that the sediment can be treated as a continuous medium, which is characterized by two phases: solids and pore water. The radionuclides of interest are assumed to be particle bound, so they are virtually absent from the pore water, and new inputs are ideally deposited on the sediment-water interface (SWI) over the previously existing material. Scenarios with non-ideal deposition have been described by Abril and Gharbi (2012). They arise from the failure of the above assumption when inputs of radionuclides are in the dissolved phase and sediments have high porosities in their top layers (see Annex A).

The above basic assumption of a continuous medium can also fail in vegetated coastal sediments. The major difficulties arise from their high content in organic matter (OM) which represents a distinct phase due to the achronological character of its belowground production and decay (Allen, 2000), its non-negligible radionuclide concentrations, and its distinct advective transport. Thus, while the mineral fraction within the sediment may retain some chronological information, each sediment slice also contains a depth and time dependent amount of OM which may be decoupled from the chronology. This then raises questions about the estimation of accretion rates from the composite mass thickness lying between two dated horizons. A reliable understanding of how early compaction operates in saltmarshes is another key question for estimating reliable linear accretion rates (commonly used in sea level rise studies).

Arias-Ortiz et al. (2018) pointed out the effect of OM decay in the increase of ^{210}Pb concentrations in the composite sediment matrix, but they did not account for belowground production, among other simplifying assumptions. Boyd et al. (2017) distinguished among mineral sediment and organic matter accumulation rates. But the above works still used the composite concentrations in the CF-CS model.

This paper is aimed at reviewing and tuning, the methodology for the ^{210}Pb-based radiometric dating of vegetated coastal sediments, specifically saltmarshes, focussing on the mineral fraction as the physical carrier of the chronological information. The work is illustrated with new data from two saltmarsh sediment cores sampled in two marshes situated on Lynher Estuary and, respectively, Tamar-Tavy Estuary (South West England).

2. Materials and methods

2.1. Regional setting

The Lynher Estuary forms a confluence with the River Tamar (Fig. 1) which in turn drains into Plymouth Sound (Natural England, 2016). The Lynher Estuary has a tidal reach of ~14 km and its coastline is dominated by upper saltmarsh communities. It is designated as a Site of Special Scientific Interest and a Special Protection Area and it has valuable salmonid and brown trout fisheries (English Nature, 2006). The land surrounding the Lynher is mainly under grass and accommodates rough grazing with mixed arable and dairy farming. The Tamar-Tavy Estuary is microtidal and flood dominant, reaching a spring tidal range of ~6.5 m. It is surrounded by mudflats and salt marshes in its lower and middle section, being granted a number of nature conservation designations for the richness of its natural diversity.

The catchments of the rivers Lynher, Tamar and Tavy had experienced extensive metal mining for metals during the 18th and 19th centuries (Dines, 1956). Mining in the region reached its peak in the 19th century but had largely ceased by 1950, leaving piles of mine waste near adjacent rivers or channels providing contaminated fine sediments into the local rivers and streams over time (Mighanetara et al., 2009).

The factors taken into account when choosing a representative saltmarsh sampling area were primarily the longevity (>100 years) of the habitat, which was obtained from historical maps collections, the extent and stability of the saltmarsh, the potential for undisturbed sediment accretion and accessibility for sampling.

Antony Marsh, lying on the southern bank of the Lynher, is a large, unaltered expanse of saltmarsh in the Lynher/Tamar riverine complex, divided by the main creek channel. Bere Ferrers Marsh is an embayment marsh, laying on the western bank of Tavy river (Fig. 1). Historical maps of Tamar/Lynher estuarine system (Ordnance Survey, 1809) show that in 1809, the two marshes were not mapped, while the marshes appear on the maps from early 20th century (Edina Digimap collection UK, 2015). The marshes may have formed, or expanded, in the middle of 19th century, during a period of increased sediment availability from mining operations in the upper catchments of the Lynher/Tamar riverine system and in the period that followed their cessation.

Both marshes have typical halophytic vegetation near the foremarsh e.g. common cordgrass (*Spartina anglica*) and common saltmarsh-grass (*Pucinella maritima*) (Fig. S1, in electronic supplementary material -ESM), having a cliff at their seaward margins.

2.2. Sampling, sample treatment and physical measurements

Two sampling sites were chosen on stable ground in the middle of Antony Marsh and Bere Ferrers Marsh, respectively at reasonable distance from the creek channel (see Fig. S1, in electronic supplementary material - ESM).

Depth continuous sediment sequences of 45 cm (Antony Marsh) and 29 cm (Bere Ferrers), respectively, were collected in the form of two monoliths, representing the side wall of a pit. This sampling strategy was appropriate i) for the collection of the OM–rich upper sediment layers without disturbance, ii) for the avoidance of compaction while sampling, and iii) for obtaining sufficient material of the upper sediment layers for laboratory analysis.

The monolith cores were stored at −20 °C and subsequently processed in a clean laboratory environment (Fig. S2a, in ESM). The monolith sequences were sectioned in 1 cm layers under partially-frozen conditions, which allowed the better processing of the porous material rich in organic matter. Distinct stratigraphic zones (Fig. S2, in ESM) were observed during the processing of the monolith cores, both with an

Fig. 1. Location map of Antony Marsh, Lynher estuary, and Bere Ferrers Marsh, Tavy estuary (South-West England). Other saltmarshes on the upper estuary of Lynher (Treluggan Marsh and Port Eliot Marsh) and lower estuary of Tamar (South Tamar Marsh) are also indicated.

upper zone (up to 18 cm and 8 cm depth, respectively) with a rich rooting system.

The sample processing included freeze-drying, weighing, fine grinding, and sieving to a particle size of <1 mm. The moisture content of each sample was determined by the difference between its wet (m_{ws}) and dry (m_s) weight. The dry bulk density values, ρ_b, were estimated by dividing the total dry weight, m_s, by the volume of each centimetre sediment layer:

$$\rho_b = \frac{m_s}{V} \tag{1}$$

For saline pore-fluids m_s^* is the corrected value of m_s by subtracting the amount of precipitated salts. The corrected ρ_b^* is derived as following (Dadey et al., 1992):

$$\rho_b^* = \rho_b \phi_s \; ; \; \phi_s = \frac{m_s^*}{m_s} = \left(1 - \frac{s\, m_{ws}/m_s}{1-s}\right) \tag{2}$$

where s is the fraction (in weight) of salts in the pore fluid. It is also useful defining f_w as the fraction in weight of water ($f_w = (m_{ws} - m_s)/m_{ws}$).

2.3. Organic carbon (OC) and loss on ignition (LOI)

Homogenized sub-samples of every third 1 cm slice were pre-treated with 0.1 M HCl to remove inorganic carbon. Dried sub-aliquots were encapsulated in pre-weighed Sn foil cups, re-weighed when packed and measured for organic carbon content (Shimadzu TOC-V Analyser). Calibration was performed using L–Cystine (30% carbon content), while the Certified Reference Material PACS–1 (National Research Council of Canada) was utilized as Quality Control (QC). An average of three replicate measurements of the PACS–1 gave a relative difference of 2.9% by comparison with the certified value.

Organic matter content was determined by the Loss-On-Ignition (LOI) method. Every third sample from both monolith cores was analysed for both LOI and organic carbon. Prior to ignition, sediment samples and empty ceramic crucibles were preconditioned by oven-drying at 105 °C overnight. Ignition of ~1 g of sample material was undertaken in a muffle furnace at 440 °C for 3.5 h (following the British Standard BS 1377–3:1990: Methods of test for soils for civil engineering purposes. Chemical and electro-chemical tests). A QC sample of known LOI was included in the sample batch. Three samples were prepared in triplicate given the heterogeneous appearance of the material and mean and relative standard deviation (SD) values were determined for these

samples. Relative SD ranged from 2.0% to 4.6% (later value given for the first sediment layer). The OM content was calculated as the difference in weight before and after the ignition.

2.4. Radionuclide measurements

Gamma-ray energies at 46.5 keV, 351.9 keV, 661.6 keV and 59.5 keV were evaluated for the determination of ^{210}Pb, ^{214}Pb (assumed to be in secular equilibrium with its parent ^{226}Ra) and ^{137}Cs and, where possible, ^{241}Am, in saltmarsh sediments for radiometric dating. Homogenized sub-samples of grain-size <1 mm were placed into individual aluminium containers (inner diameter 47.50 mm, filling height to the rim 15.00 mm) or into high density polyethylene vials (inner diameter 12.25 mm, filling height 41.3 mm) depending on the available sample mass, compressed and sealed with glue and electrical tape.

Gamma-ray measurements begun after incubation for four weeks during which secular equilibrium was achieved between ^{222}Rn and its progenies (e.g. ^{214}Pb). Two Ortec gamma detectors (Ortec, Wokingham, UK) were used for the gamma measurements: an n-type coaxial HPGe detector, with 50% relative efficiency, and a well HPGe detector. Counting live time was set to approximately 48 h to achieve a statistically significant number of counts and a counting statistics of about 10% or less for the 46.5 keV photopeak. Special care was taken to maintain these standard counting conditions for all samples.

The commercially available software (GammaVision, Ortec) was used for data acquisition, while data analysis was performed in EXCEL, in combination with Monte Carlo simulation using EFFTRAN (Vidmar, 2005). The detector efficiency was calibrated over the energy range 46.5–1836 keV using a secondary standard soil material in the same geometry as the samples. The standard was created by spiking a soil material of known chemical composition with a gravimetrically-determined quantity of a multi-gamma standard solution (Eckert and Ziegler; traceable to the National Institute of Standards and Technology - NIST). The efficiency transfer approach and EFFTRAN derived efficiency transfer factors were employed to account for differences in chemical composition between the soil standard and saltmarsh samples (Iurian et al., 2018).

The chemical composition of the sample matrix, used to derive the efficiency transfer factors, was determined by Wavelength Dispersive X-Ray Fluorescence (WD-XRF) in pressed pellets, using a state-of-art PANalytical XRF Spectrometer and dedicated software for data interpretation. The accuracy of the XRF results was checked by repeated measurements (n = 3) of the CRM SdAR-M2, a metal-rich sediment (US Geological Survey). The maximum deviation from the reference values was 8%.

Activity concentrations were decay-corrected to the sampling date and corrected for background fluctuations and moisture content, the latter estimated by oven-drying about 1 g of material at 105 °C. The activities are reported with their combined standard uncertainties at a 1σ confidence level, determined according to the Guide to the Expression of Uncertainty in Measurement JCGM 100:2008 (JCGM, 2008).

Quality control was undertaken using IAEA Proficiency Test Materials with similar matrix characteristics to the Antony sediment samples (e.g. IAEA-CU-2009-03 moss-soil and IAEA-TEL-2016-03 soil). External quality control is assured by regular laboratory participation in external proficiency tests: e.g. IAEA (international); National Physical Laboratory (United Kingdom), Max Rbner Institute Karlsruhe (Germany).

2.5. ^{210}Pb-based radiometric dating models adapted to vegetated saltmarsh sediments

2.5.1. Mass flows in saltmarsh sediments and the continuity equation

Flows of solids onto the saltmarsh sediment-water interface (SWI), or onto the sediment-atmosphere interface–under unsaturated conditions, consist of mineral or inorganic particles and detrital organic matter from plant tissues and other inputs associated with suspended loads and continental runoff (see the review by Allen, 2000). The composite flow of matter ensures the sediments undergo an ordered growth in time. Nevertheless, plant roots, rhizomes and tubers grow 'in-situ' because of non-localized photo-assimilation (biological compounds produced by photosynthesis). They occupy the pore spaces and become the major contributor to sediment structure in the rhizosphere. This contribution from below ground biomass represents a depth-distributed input of matter which is independent from the ages ascribed to any sediment horizon. Fig. 2 illustrates the root zone in vegetated salt-marsh sediments and the two-mass flow components.

The below ground productivity of *Spartina,* a common type of vegetation in saltmarshes, has shown to vary between 0.34 and 6.04 kg m^{-2} a^{-1} (dry weight) being broadly similar for other species (Allen, 2000). In the absence of decay, the productivity range above is equivalent to a linear accretion rate of 1–10 mm a^{-1} (Allen, 2000). These figures are increased by above ground productivity and allochthonous inputs. Nevertheless, a significant proportion of the organic material introduced below ground eventually decays as the result of bacterial and fungal processes, the activities of invertebrate grazers, and the presence of oxygen and moisture, with decay rates largely depending on several factors (Allen, 2000). Values of 12–50% per year have been reported for *Spartina* in the upper few decimetres of the saltmarsh sediments (Allen, 2000), where unsaturated conditions often prevail. The decay rate of OM decreases as the sediment becomes permanently waterlogged and anoxic conditions prevail. Consequently, the OM is mineralized by an anaerobic food chain whose final by-products are carbon dioxide and methane (Middelburg et al., 1993).

The bulk density (Eqs. (1) and (2)) can be divided into its organic ($\rho_{b,\,org}$) and mineral ($\rho_{b,\,min}$) components.

$$\rho_{b,\,org} = f^{*}_{org}\rho^{*}_{b} = f_{org}\rho_{b},\ \rho_{b,\,\min} = \rho^{*}_{b} - \rho_{b,\,org} \tag{3}$$

where $f_{org} = m_{org}/m_s$, with m_{org} being the mass of organic matter (determined by LOI), and $f^{*}_{org} = f_{org}/\phi_s$ is its salt-corrected value.

The mass depth $m(z)$ is the dry mass per unit area accumulated from the SWI until the sediment horizon, which during the slicing operation is at actual depth z. It is the physically meaningful depth-scale for radiometric dating since it remains invariant under natural compaction and

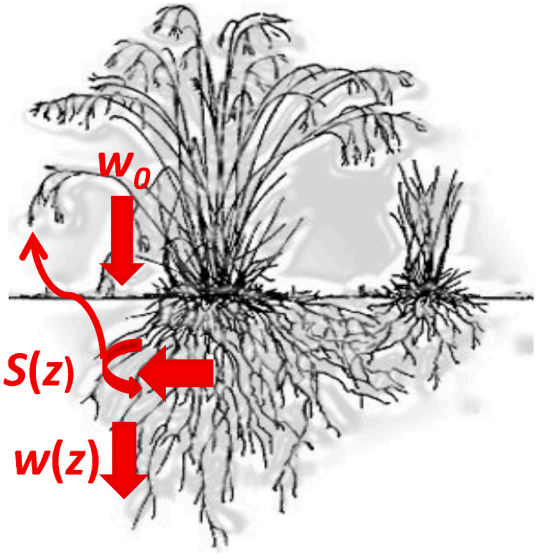

Fig. 2. Sketch illustrating the root zone in vegetated salt-marsh sediments and the two-mass flow components: i) w_0 is the flow of solids entering through the sediment-water/atmosphere interface, and ii) $w(z)$ is the composite mass flow, which results from the one above and $S(z)$; this last is the net balance of root growth from non-localized photo-assimilation and the mineralization rate with gaseous exchanges.

the sediment shortening during coring, storage and extrusion operations. The organic ($m_{org}(z)$) and mineral ($m_{min}(z)$) mass-depth scales can be defined as follows:

$$m(z) = \int_0^z \rho_b(z')dz' ;\ m_{org}(z) = \int_0^z \rho_{b,\ org}(z')dz' \ ;\ m_{min}(z) = \int_0^z \rho_{b,\ min}(z')dz' \tag{4}$$

The continuity equation for bulk density, ρ_b, expressing the mass conservation for solids in non-vegetated sediments is (Abril, 2003):

$$\frac{\partial \rho_b}{\partial t} = -\frac{\partial w}{\partial z} \tag{5}$$

Eq. (5) applies to a reference framework located at the SWI, with depth z measured positive downwards. At any time, and at the sediment horizon at depth z, the flow of matter, w (z,t) [M L^{-2} T^{-1}], can be written in terms of the linear accretion rate, v (the velocity at which the SWI displaces vertically due to overall processes contributing to sediment accretion) plus the relative velocity of solids with respect to a fixed (at rest) framework, q. Thus,

$$w(z,t) = [v(t) + q(z,t)]\rho_b(z,t) \tag{6}$$

The flow of matter driven by the compaction potential vanishes at the early compaction limit (ECL), where the bulk density reaches a virtually constant value $\rho_{b,ECL}$ (Abril, 2003, 2011). Then, from Eq. (6):

$$w(z_{ECL}, t) = v(t)\ \rho_{b,ECL} \tag{7}$$

The steady state solution of Eq. (5) $\left(\frac{\partial \rho_b}{\partial t} = 0\right)$ implies that the mass flow, w, is constant with depth z. Then the mass flow at the SWI, w_0, usually known as SAR, satisfies the relationship:

$$w_0 = v\ \rho_{b,ECL} \tag{8}$$

In vegetated saltmarsh sediments Eq. (5) can be generalized by separately applying it to the mineral and the organic phases, and by including the depth-dependent net balance of below-ground production and decay, labelled as s(z) [$ML^{-3}T^{-1}$]:

$$\frac{\partial \rho_{b,min}}{\partial t} = -\frac{\partial w_{min}}{\partial z} = -\frac{\partial}{\partial z}\left(\rho_{b,min} v + \rho_{b,min} q_{min}\right) \tag{9a}$$

$$\frac{\partial \rho_{b,org}}{\partial t} = -\frac{\partial w_{org}}{\partial z} + s(z) = -\frac{\partial}{\partial z}\left(\rho_{b,org} v + \rho_{b,org} q_{org}\right) + s(z) \tag{9b}$$

Importantly, the linear accretion velocity of the SWI is the same for both components. Here the terms $q_{\min}$ and q_{org} can be interdependent, following a more complex law than that reported by Abril (2011), but which falls beyond the scope of the present work. In general, they will take different values, and thus, the chronological information eventually attached to the detrital OM entering through the SWI advances at a different rate when comparing with mineral solids. Moreover, the term s (z) breaks down any chronological information attached to the OM as a whole. Although the situation is complex, it is possible to get some helpful insights from the above physical fundamentals.

Below the rhizosphere, a physical environment of water pores and solids of uniform density is progressively re-encountered, allowing for an ECL. Let us assume that by some means, ages t_1 and t_2 have been estimated for the mineral fraction at the sediment horizons z_1 and z_2. The amount of mineral matter per unit area (mineral mass thickness) comprised between both horizons, Δm_{min}, can be empirically determined. The mean value of the mineral SAR between the above two ages is $w_{\min} = \Delta m_{min}/\Delta t$; with $\Delta t = t_2 - t_1$. When after some elapsed time this material reaches the ECL, it will be bounded by horizons at depths z_1' and z_2', with the same absolute difference in ages, Δt, but with $dz' = z_2' - z_1' < dz = z_2 - z_1$ due to self-compaction. Thus, the ratios $dz'/\Delta t$ and $dz/\Delta t$ only describe the state (in terms of early compaction) of the mineral mass thickness Δm_{min} at different times of observation (or different times of sediment sampling), and they are not describing the linear accretion velocity of the SWI at any time. At the ECL the mass-flow $\rho_{b,min} q_{min}$ vanishes, and it can be said that $w_{\min}$, a former mass flow at the SWI, will finally produce a linear accretion velocity of the SWI given by

$$v = w_{min} / \rho_{b,min,ECL} \tag{10}$$

The effect of plant growth is reflected in the OM content beyond the ECL, which competes with the mineral fraction for the bulk volume leading to lower values of $\rho_{b,min,ECL}$ than in OM-free sediments, and then to higher v values.

2.5.2. *Radionuclides in sediments and transfer to plants*

Radionuclides uptake by plants has been extensively studied for the soil-plant system, and it is described as a series of two processes: (1) radionuclides partition between soil and soil solution (defined by the partition coefficient, K_d), and (ii) radionuclides uptake by plants from the soil solution (defined by the Concentration Ratio (*CR*) parameter as the ratio between activity concentration in plant material and the one in the substrate – typically at the rooting zone i.e. approximately the upper 10 cm layer for grasses –e.g., see IAEA, 2010).

A compilation of literature data on concentration ratios (*CR*) for some radionuclides of interest in radiometric dating has been made (Table 1), and directly compared with site and plant specific data from estuarine saltmarshes in Plymouth Sound (SW, England). Concentration ratios (*CR*) of ^{210}Pb and ^{226}Ra for UK saltmarsh plants seem to be comparable with the TRS 472 (IAEA, 2010) generic values for grasses (stems and shoots) and 2–3 fold higher than rice mean values (under flooded conditions) (Table 1). A significant positive correlation (Pearson Correlation Coefficient $r = 0.919$, $p < 0.001$) was found between ^{137}Cs *CRs* and organic matter (%) (Sanchez et al., 1999). However, the difference in *CR* values seems to be significant only for very high OM content (OM $\geq$ 90%) (see Table 1).

Any sediment sample with dry mass m_s is composed by a mass $f_{org}\ m_s$ of organic matter and a mass $[1 - f_{org} - (1 - \phi_s)]m_s$ of mineral mater (without salts). If they could be physically divided, the studied radionuclides would be bound to these fractions with activity concentrations A_{org} and A_{min}, respectively, but in practice we measure the activity concentration A_b in the bulk (composite) sediment sample. The following relationship follows from the above definitions:

Table 1
Radionuclide concentration ratios, *CR* (geometric means), for ^{226}Ra, ^{210}Pb, ^{137}Cs, ^{241}Am (dimensionless).

Vegetal tissue	^{226}Ra	^{210}Pb	^{137}Cs	^{241}Am
Aerial plant (saltmarshes UK)[a]	**2.0×10^{-1}**	**3.5×10^{-1}**		
Rice[b]	8.7×10^{-4}	8.4×10^{-3}	8.3×10^{-3}	
Root crops (roots)[b]	7.0×10^{-2}	1.5×10^{-2}	4.2×10^{-2}	6.7×10^{-4}
Root crops (stems and shoots)[b]	7.1×10^{-2}	6.3×10^{-2}		
Grasses (stems and shoots)[b]	1.3×10^{-1}	3.1×10^{-1}	6.3×10^{-2}	3.3×10^{-2}
Grasses (stems and shoots); organic substrate (OM $\geq$ 20%)[b]			2.8×10^{-1}	
Grasses; organic substrate (OM $\geq$ 90%)[c]			3.6–4.4 (x 10)	
Grasses; organic substrate (OM 48%, clay 6.1%)[c]			7.4×10^{-1}	

[a] Geometric mean of two values (authors' personal data from estuaries of SW England).
[b] IAEA (2010).
[c] Sanchez et al. (1999).

$$A_b = \frac{A_{min}\left(1 - f_{org} - (1-\phi_s)\right)m_s + A_{org} f_{org}\, m_s}{m_s} = A_{min}\left(1 - f_{org} - (1-\phi_s)\right) + A_{org} f_{org} \tag{11}$$

At this point, and in absence of more precise determinations of the ratio A_{org}/A_b, we will assume that it can be approached by a reference *CR* value (Table 1). The best choice for *CR* could be a site and plant specific value, preferably determined from root tissues. This could be thought to be a first order approach due to the varying contributions to OM (living tissues and detrital) at different sediment depths. It will be shown below that this approach can be reliable in the tuning radiometric dating models, mainly because of the low order of magnitude of *CR*.

This approach allows estimating A_{min} from Eq. (11) in terms of the experimentally measured A_b:

$$A_{min} \cong \frac{A_b\ \left(1 - CR\, f_{org}\right)}{1 - f_{org-(1-\phi_s)}} \tag{12}$$

The partitioning of the studied radionuclide between the mineral and organic phases can be quantified. In a sediment sample of mass m_s, the activity contained in the mineral component is $A_{\min}\ [1 - f_{org} - \ (1 - \phi_s)]\ m_s$ while the total radionuclide activity is $A_b\ m_s$, and their ratio is (from Eq. (12)) $1 - CR\ f_{org}$. Thus, in the case of ^{210}Pb, when using the *CR* value for plant bodies in UK saltmarshes (Table 1), and with $f_{org} = 0.5$, it results that 82.5% of the activity is bound in the mineral phase.

Thus, when A_b is used instead of $A_{\min}$ (which is the one linked to the chronological information), the major effect of a high OM content is a dilution, or a decrease, of A_b (i.e. the flattening in A_b often observed in the upper sediment layers occupied by the rhizosphere). This can lead to spurious SARs and chronologies.

Equation (12) can be assessed using different values of *CR* and f_{org} to conclude that for *CR* of an order of 10^{-1} the dominant effect in the $A_{\min}/A_b$ ratio is the 'dilution' given by f_{org}. Furthermore, sensitivity tests will be conducted in the next sections for assessing the effect of a range of values for the *CR*, situated within 1.5×10^{-2} and 3.0×10^{-1}.

3. Results

Tables S1 and S2, in the supplementary material, report the raw results from physical measurements (section 2.2), OC and LOI (section 2.3), and radionuclide mass activity concentrations (section 2.4) for the Antony Marsh and Bere Ferrers cores, respectively.

3.1. Bulk density, OM and LOI

Fig. 3 shows the results of the water content for both cores, along with bulk densities estimated by (Eq. (1)) and (Eq. (2)), by using $s = 0.025$ according to the values reported by Ralph (1956) for interstitial salinities of intertidal muds at several locations along the Tamar Estuary. Correction by Eq. (2) implies a maximum absolute deviation of 0.03 g cm^{-3}, or a maximum relative deviation of 13.9% (data for the Antony Marsh core). Note that propagated relative uncertainties of about 5–10% can be expected in the estimation of bulk density (Eq. (1)), mainly contributed by the associated uncertainties in the bulk volume of the samples. Fig. 3 also reports the percentages of clay + silt (particle sizes < 63 μm) determined for each sediment slice in the two studied cores.

Twelve samples from the Antony Marsh core, in the range 0–45 cm, have been measured for C_{org} (%) and LOI (%) to establish a site-specific linear regression, together with data on their silt + clay fraction (<63 μm). The clay content of the samples ranged from 1.8% to 3.6% and silt was the major constituent.

A multiple linear regression analysis (LOI versus C_{org} and particle sizes < 63 μm) was conducted using Statgraphics Centurion XVI. LOI (%) showed a significant positive correlation with C_{org} (%), $r = 0.917$, but no significant correlation with the silt + clay fraction. An atypical residue

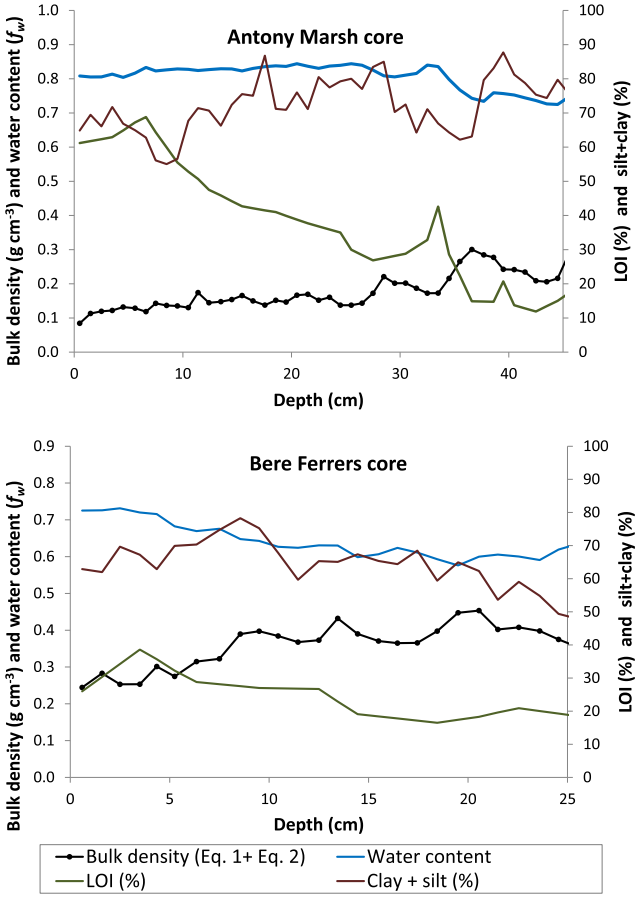

Fig. 3. Water content (given as the fraction f_w), bulk density, LOI (%) and percentage of clay + slit (particle sizes < 63 μm) in the Antony Marsh and the Bere Ferrers cores.

was found for data from the uppermost sediment slice, which also showed a high relative standard deviation in the replicated analysis (see Table S1). When discarding this point, the correlation coefficient LOI versus C_{org} was $r = 0.946$, with $p < 0.001$. The regression equation being:

$$\text{LOI}(\%) = -2.68 + 2.94\ \text{Corg}(\%) \tag{13}$$

The intercept is compatible with zero, since it is affected by a standard error over 100%. The slope (2.94 ± 0.34) is noticeably higher than the van Bemmelen factor of 1.724, but comparable to the factor 2.41 inferred from the correlation reported by Kauffman and Donato (2012) for mangrove forest sediments. High precision (RSD, 1.2%) in TOC on LOI prediction was found by De Vos et al. (2005) in forest floor samples with high organic matter content (LOI > 5%).

In the Antony Marsh core, C_{org} (%) was determined for ~33% of the samples. For the non-measured slices, linear interpolations were used to complete the record. LOI (%) was determined for 33% of the samples in the 0–25 cm depth range, and for various slices at greater depths. For the non-measured sediment slices, linear interpolations were used in the 0–25 cm depth range, and the empirical Eq. (13) for the rest (Fig. 3). For the Bere Ferrers core it has been assumed that Eq. (13) can be applied for estimating LOI(%) from the C_{org} (%) values. Linear interpolations were used for completing the LOI(%) record (Fig. 3).

3.2. Results on ^{137}Cs: preservation of the chronological information and STA model

Fig. 4 shows the ^{137}Cs activity concentrations in the composite sediment versus depth in the two studied sediment cores. The salt-corrected ^{137}Cs activity concentrations in the mineral fraction (after Eq. (12)) are also depicted for $CR = 1.0 \times 10^{-2}$ and $CR = 1.0 \times 10^{-1}$, and using $s = 0.025$. In both cases, a well-defined ^{137}Cs peak is observed. This is commonly accepted as a confirmation of the preservation of the chronological information.

Applications of ^{137}Cs as a chronostratigraphic marker in saltmarsh sediments can be found, among others, in Cundy and Croudace (1996); Bellucci et al. (2007); Leorri et al. (2008) and García-Artola et al. (2016).

Estimations of ^{137}Cs concentrations in the mineral fraction in the two cores (after Eq. (12)) reveal that the dilution effect by OM is quite noticeable, being higher in the Antony Marsh core because its higher OM content (Fig. 3), and that here the accurate estimation of the *CR* factor plays a minor role.

It is worth noting that none of the ^{137}Cs versus depth profiles in Fig. 4 is a mirror-image of the atmospheric deposition record (see Fig. S3, in ESM). Particularly, concentrations in recent years (upper sediment slices) are much higher than expected. However, this is a common feature in most of the sedimentary systems, and the system-time-average (STA) model (Robbins et al., 2000, and Annex A) attempts to account for this effect.

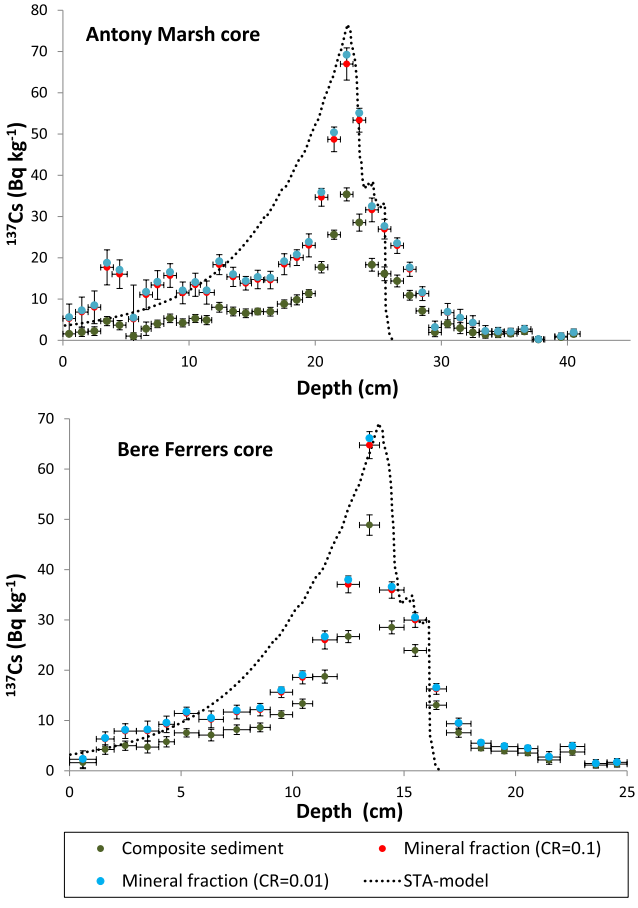

Fig. 4. ^{137}Cs activity concentrations (in the composite sediment) versus depth in the two studied sediment cores. ^{137}Cs activity concentrations in the mineral fraction have been estimated after Eq. (12) for $CR = 1.0 \times 10^{-2}$ and $CR = 1.0 \times 10^{-1}$. In both cases vertical error bars are 1σ analytical uncertainties (omitted for $CR = 1.0 \times 10^{-2}$ for graphical clarity), while horizontal bars delimit the depth interval of the measured sediment slice. The predicted profiles in the mineral fraction after the system-time-average (STA) model (Robbins et al., 2000; Annex A) are also depicted.

The best fit of the STA model for ^{137}Cs in the mineral fraction of the two cores (by using the atmospheric deposition record from Fig. S3, ESM, data from Wright, 2016) is depicted in Fig. 4. The time parameter is $k_r = 0.068$ a^{-1} for Antony Marsh, and $k_r = 0.070$ a^{-1} for Bere Ferrers cores. These values are comparable to others reported in the scientific literature (e.g., Robbins et al., 2000; Abril et al., 2018).

The STA model approximates to the observed recent ^{137}Cs activity concentrations, which are higher than expected from atmospheric deposition. Consequently, it can be concluded that recent ^{137}Cs fluxes onto the SWI must be governed by the ^{137}Cs activity concentration attached to the (mineral) mass flow entering into the SWI. Additionally, the ^{137}Cs profiles in the sediments extend deeper than expected from the STA model. This can be explained by the non-ideal deposition of ^{137}Cs fallout reaching the SWI shortly after the bomb-fallout peak (see Annex A).

From the data in Tables S1 and S2, the total ^{137}Cs inventory for the Antony Marsh core is $\Sigma_{Cs} = 545 \pm 13$ Bq·m^{-2}, and 1032 ± 12 Bq·m^{-2} for the Bere Ferrers core, while the integrated atmospheric deposition at the site, decay-corrected to the date of sampling is 355 ± 38 Bq m^{-2} (error estimates from a uniform relative standard deviation of 16% for each annual data). Thus, Σ_{Cs} is greater than the integrated atmospheric deposition. This agrees with the notion of inputs onto the SWI being governed by the mass flow from the catchment.

3.3. Varying ^{210}Pb$_{exc}$ fluxes onto the SWI

The widespread use of the Constant Rate of Supply (CRS) model has resulted in the general acceptance of the assumption of a constant rate of supply as the paradigm describing the functioning of natural aquatic ecosystems. Nevertheless, in all those cases where it has been possible to reconstruct ^{210}Pb$_{exc}$ palaeofluxes onto the SWI (e.g., in varved sediments for which an independent chronology is available), they show large variations over time and a positive correlation with SAR (Abril and Brunskil, 2014). A more detailed discussion of the two mass-flow components with intrinsic scatter (the conceptual model which explains the available empirical evidence) can be found in the above reference.

Fig. 5 shows the ^{210}Pb$_{exc}$ and ^{137}Cs inventories in five vegetated saltmarshes sediment cores sampled at different locations within the same Plymouth Sound estuarine environment (UK), plotted versus the SAR value estimated from the composite mass depth and the position of the ^{137}Cs fallout peak ascribed to 1963. Here the estimation of SARs can be considered only as a proxy, but the fundamental fact is the positive

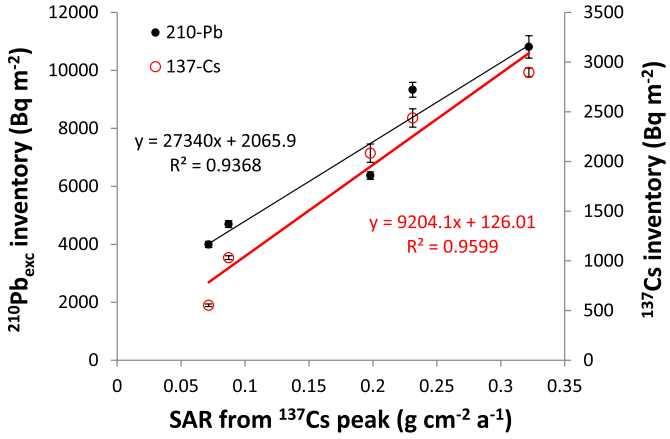

Fig. 5. Measured ^{210}Pb$_{exc}$ and ^{137}Cs inventories in five saltmarsh sediment cores from the Lynher estuary (see Fig. 1) versus the SAR value estimated from the composite mass depth and the position of the ^{137}Cs fallout peak ascribed to 1963 (data from authors personal records).

correlation between inventories (related with fluxes onto the SWI) and SARs, which are consistent with results by Abril and Brunskil (2014) and the above insights from ^{137}Cs.

3.4. Fine-tuning radiogeochronological models for vegetated saltmarsh sediments

The key idea for adapting the existing radiometric dating models is the use of specific activity concentrations in the mineral phase (A_{min}) and the mineral mass depth scale. Determining the mineral mass depth is quite straightforward (Eq. (4)), whereas the former requires further methodological treatment (including the physical separation of the mineral phase). As discussed in Section 2.5 and owing to the relatively low values of *CR* reported in Table 1, the application of Eq. (12) on a local basis can provide a reasonable proxy for $A_{\min}$. This will be the approach adopted in what follows. Since the aim is a methodological development, rather than an in-depth discussion of the case study, the $CR = 7.0 \times 10^{-2}$ value was adopted for ^{226}Ra, as the reference value for roots of root crops from the IAEA TRS 472, reported in Table 1. For ^{210}Pb the sensitivity of results was tested using extreme *CR* values of 1.5×10^{-2} and 3.0×10^{-1}, corresponding, respectively, to root crops, and to grasses and aerial parts of the plants in the studied saltmarshes (Table 1).

Fig. 6 shows the ^{210}Pb$_{exc}$ profiles for the two studied cores, with mass activity concentrations referred to the composite sediment and to its mineral fraction, the latter being estimated for the above two *CR* values.

The depth distribution function of ^{210}Pb$_{exc}$ has a major importance in establishing a chronology. Estimations of ^{210}Pb$_{exc}$ concentrations in the mineral fraction in these cores (after Eq. (12)) reveal that the dilution effect by OM creates a visible variation of these concentrations with depth. The effect is higher in the Antony Marsh core because its higher OM content (Fig. 3). Sensitivity tests for *CR* reveal the importance of handling site and plant specific values. It is worth noting that other works assumed $CR = 0$ for studying the effect of OM decay in ^{210}Pb-based dating models (e.g. Arias-Ortiz et al., 2018).

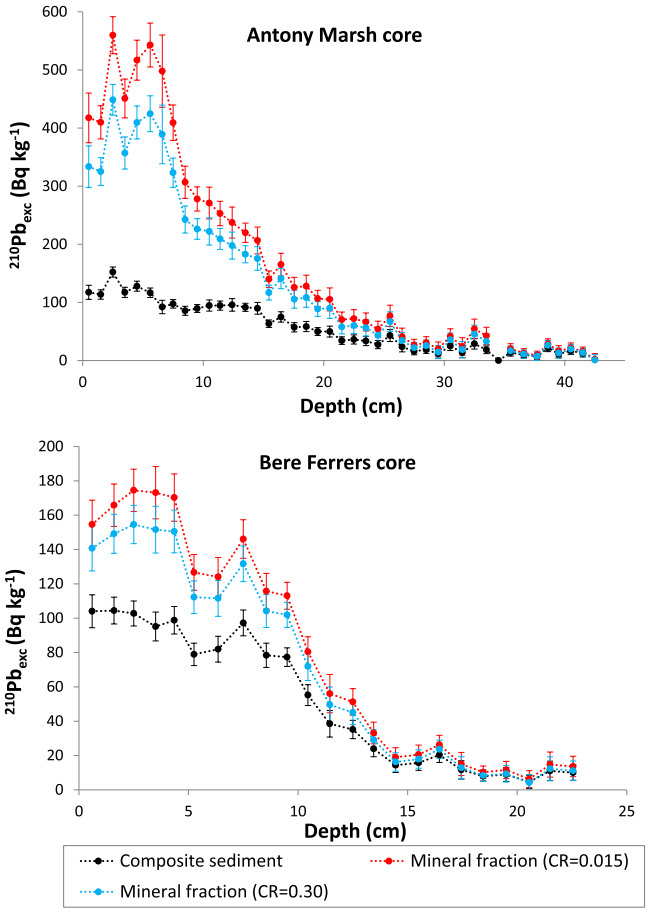

Fig. 6. ^{210}Pb$_{exc}$ vs depth (cm) in the composite sediment and its estimated values in the mineral fraction (from Eq. (12), using LOI from Fig. 3, $s = 0.025$, and $CR = 1.5 \times 10^{-2}$ and $CR = 3.0 \times 10^{-1}$) in the two studied cores. Error bars are 1σ propagated uncertainties.

3.4.1. CRS model in vegetated saltmarsh sediments

The assumptions adopted for the CRS model and its basic equations are summarized in Annex A. In vegetated saltmarsh sediments the major limitations can be: i) non-random temporal variability in fluxes (Abril, 2019); ii) the system not being old enough to ensure a steady state inventory; iii) the partitioning of the inventory into mineral and organic fractions with different mass flow rates ($w_{\min}$, w_{org} in Eq. (9)), so that Eq. A-2 is not strictly applicable. In cases where the first two limitations do not apply, the third can be surpassed when most of the activity remains bound to the mineral fraction; this is, when $CR \times f_{org} \ll 1$, as it seems to be feasible for ^{210}Pb$_{exc}$ (see Section 2.5.2). In these cases Eq. A-2 should produce close chronologies when consistently applied to both the mineral phase or to the composite sediment.

By using Eq. A-2 with the composite sediment, the computed CRS ages are depicted in Fig. 7, along with the ^{137}Cs time-mark, for the two studied cores. When using Eq. A-2 with the mineral phase with the two extreme values for *CR*, the chronologies closely match the previous ones (Fig. 7).

Linear SARs (Fig. 7) show a trend of increasing in recent years in both cores, which can be a spurious effect due to the early compaction (see Section 2.5.1) and to the contribution of achronological belowground production of OM. Physically meaningful palaeofluxes of inorganic solids (or mineral SARs) can be estimated from the mineral mass thickness and the dated horizons. Only the trend-lines or mean values of CRS-SARs over relatively large time periods have a physical meaning (Abril, 2019, 2020). For the Antony Marsh sediment core, the CRS mineral SARs post-dating the ^{137}Cs peak slightly fluctuate about a value of 0.030 g cm^{-2} a^{-1}, with large fluctuations for older layers, and a mean value of 0.043 g cm^{-2} a^{-1} over the last century. In the Bere Ferrers core, the mineral SAR also shows acceleration in recent years, which is the expected model outcome to the pronounced flattening of the ^{210}Pb$_{exc}$ profile (Fig. 6). In this core the CRS chronology does not match well the ^{137}Cs time mark (Fig. 7); this can be attributable to a weak accomplishment of the model assumptions. Particularly, the assumption of a constant flux can hardly hold under a continuous trend of increasing SAR in scenarios where the inputs of radionuclides are linked to the mass flows, as seem to be the case for these cores (Figs. 4 and 5).

Fig. S4, in ESM, shows a comparison among the chronologies produced by the CRS and the PLUM model when applied to the composite sediment in both cores. For PLUM application, the current version for Python has been used (see Annex A), with the default settings. Exception was the parameter *Al*, involved in the definition of a chronological limit (linked to the analytical detection limit), for which we tested the values $Al = 0.1$ and $Al = 5.0$. Fig. S4 plots the mean and the 95% confidence interval (dashed lines) for PLUM. The two models converge for recent ages, but PLUM overestimates older ages, slightly in Bere Ferrers core, but with strong discrepancies in the Antony Marsh core. PLUM did not fit the ^{137}Cs time mark in these cores. Its current version for Python may still need some adjustments, so no further implications are considered here.

The use of the assumption of a constant flux can be independently tested by the estimation of the equivalent constant fluxes pre- and post-dating the 1963 time-mark of ^{137}Cs from the ^{210}Pb$_{exc}$ partial inventories (e.g., Abril, 2019). For the Antony Marsh core, the estimated fluxes pre- and post-dating 1963 are 125 ± 13 Bq m^{-2}a^{-1} and 106.1 ± 2.2 Bq m^{-2}a^{-1}, respectively, whose difference is not statistically significant at 95% confidence level (Least Significant Difference (LSD) test).

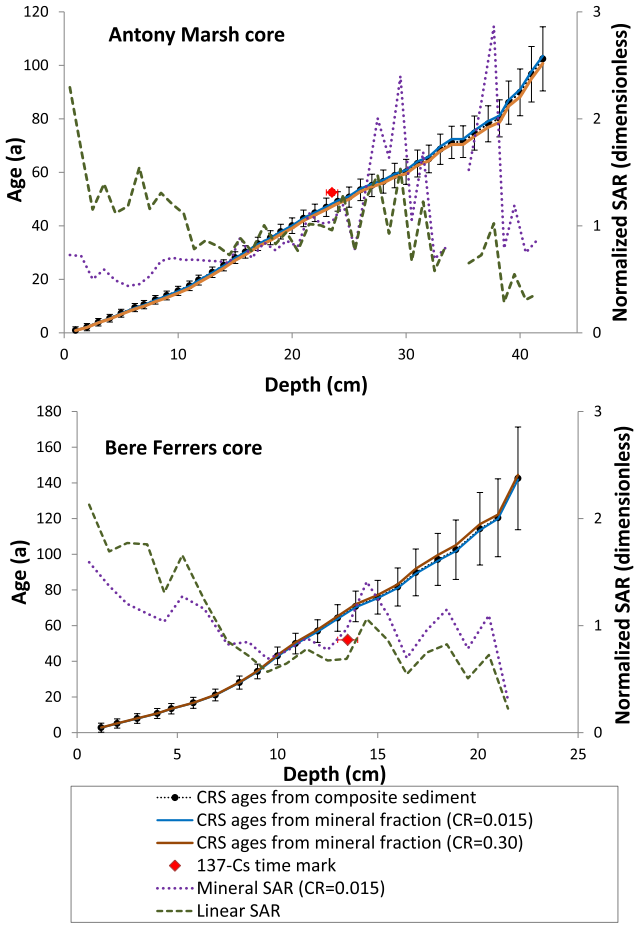

Fig. 7. CRS chronologies for the Antony Marsh and the Bere Ferrers sediment cores, as a function of depth (cm). They have been computed using Eq. A-2 with the composite sediment and with the mineral fraction using two *CR* values. The ^{137}Cs time-mark (see Fig. 4), ascribed to 1963, is also depicted. Error-bars for ages are reported only for the composite sediment. Linear SAR ($\Delta z/\Delta t$) and mineral SAR ($\Delta m_{min}/\Delta t$) are represented after normalizing to their arithmetic means in the 0–42 cm interval (0.48 cm/a and 0.043 g cm^{-2}a^{-1}, respectively) for Antony Marsh and 0–23 cm interval (0.20 cm/a and 0.048 g cm^{-2}a^{-1}, respectively) for the Bere Ferrers core. The mineral mass depth scales can be seen in Tables S1 and S2.

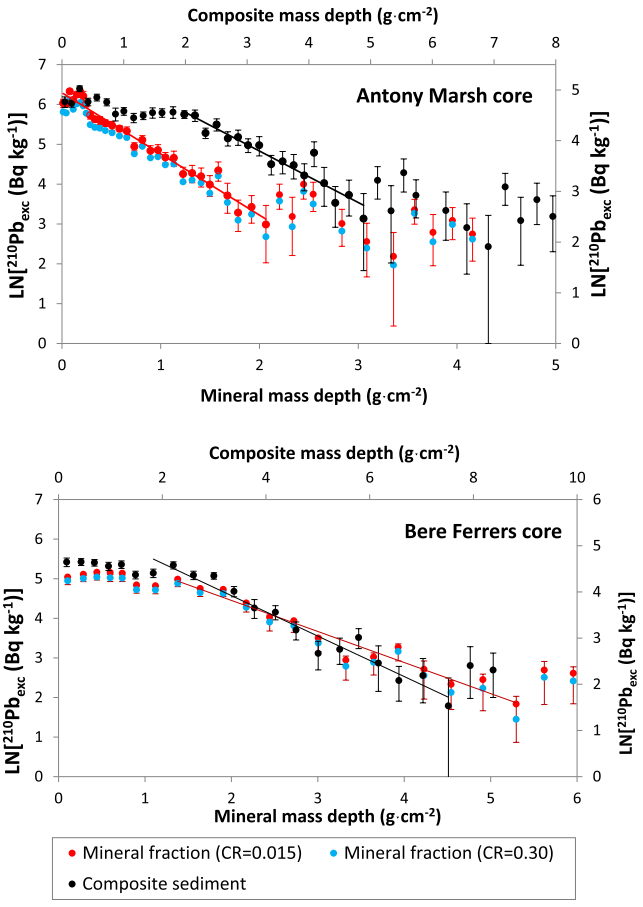

Fig. 8. Natural log of ^{210}Pb$_{exc}$ concentrations in the composite sediment and in the mineral phase for both cores (each one with its corresponding mass depth scale), and considering the two extreme values for *CR*. The straight lines are the fit of the function from Eq. A-4 to the portion of the ^{210}Pb$_{exc}$ profiles where the linear trend of decrease is apparent (the plot for $CR = 3.0 \times 10^{-1}$ is not shown for graphical clarity). Results are summarized in Table 2.

Nevertheless, for Bere Ferrers core, the equivalent constant fluxes pre- and post-dating 1963 are 76 ± 9 Bq m^{-2}a^{-1} and 134 ± 4 Bq m^{-2}a^{-1}, respectively, with a statistically significant difference at 95% confidence level (LSD test).

3.4.2. *CF–CS model in vegetated saltmarsh sediments*

The assumptions adopted for the CF-CS model and its basic equations are summarized in Annex A. Fig. 8, using a logarithmic scale, plots ^{210}Pb$_{exc}$ concentrations in the composite sediment and in the mineral phase for both cores (each one with its corresponding mass depth scale), and considering the two extreme values for *CR*. It is evident that the assumptions of the CF–CS model clearly fail in the upper and deepest portions of the cores for both mineral and composite concentrations.

A piecewise CF–CS model would interpret the flattening of the ^{210}Pb$_{exc}$ profiles in the upper portion of the cores as the result of very high SARs, as in the case of a single depositional event, what seems unrealistic for these cores.

Eq. A-4 has been fitted to the portions of the ^{210}Pb$_{exc}$ profiles shown in Fig. 8, where a linear trend of decrease is quite apparent. SAR values (-λ/slope) can be estimated from these fits and compared with the average SAR value post-dating the 1963 peak in ^{137}Cs fallout (see Tables S1 and S2). Results are summarized in Table 2.

Although the application of the CF-CS model to the composite sediment leads to numeric values for SAR, they do not have a physical meaning, since sediment masses and their activity concentrations are accompanied by a varying amount of 'achronological' organic matter, as explained above. Since mineral SARs have been estimated only for a portion of the core, several constraints must be noted: i) the mean SAR value does not apply to the entire core, nor to the entire portion post-

Table 2
SAR values estimated from the CF-CS model and the ^{137}Cs peak for the Antony Marsh and the Bere Ferrers cores.

SAR	Antony Marsh (g cm^{-2}a^{-1})			Bere Ferrers (g cm^{-2}a^{-1})		
Composite SAR from ^{137}Cs (post-dating 1963)	0.0719	±	0.0018	0.088	±	0.004
Composite SAR from fit to Eq. A-4	0.049	±	0.004	0.065	±	0.005
Mineral SAR from ^{137}Cs (post-dating 1963)	0.0270	±	0.0009	0.058	±	0.003
Mineral SAR from fit to Eq. A-4 ($CR = 0.30$)	0.0205	±	0.0007	0.043	±	0.004
Mineral SAR from fit to Eq. A-4 ($CR = 0.015$)	0.0202	±	0.0007	0.045	±	0.004

For all fits $p < 0.001$, with R^2 in the range (0.89, 0.99).

dating the ^{137}Cs peak; ii) although a relative chronology could be built up from the estimated SAR value, it is not an absolute one, since the age at the start end of the transect has not been solved from CF–CS model; iii) the quality of the fit does not warrant the confidence of the chronology.

After Fig. 6, the use of the CF-CS model in saltmarshes sediments with high OM content is only physically meaningful when applied to the mineral fraction and using the mineral mass depth scale. For the two studied cores the CF-CS is not a good model choice because the mean value of fluxes and/or SARs changes over time (as shown for the Bere Ferrers core with the support of the ^{137}Cs time mark).

3.4.3. *CIC model applied to vegetated saltmarsh sediments*

The assumptions adopted for the CIC model and its basic equation are summarized in Annex A. A physical scenario with initial activity concentrations and SAR values independently and randomly varying around their respective mean values can be suitable for a CIC model, but the meaningful chronological line is the trend-line defined by the CIC ages, which are estimated after stating the value of the initial activity concentration (Abril, 2020). The chronological information is kept in the specific activity concentration in the mineral fraction.

Fig. 9 shows the result of CIC application (Eq. A-3) to the two studied cores and with the two extreme values of *CR* for estimating ^{210}Pb$_{exc}$ concentrations in the mineral fraction. The model is also applied to the composite sediment for comparison. Model results depend on the choice

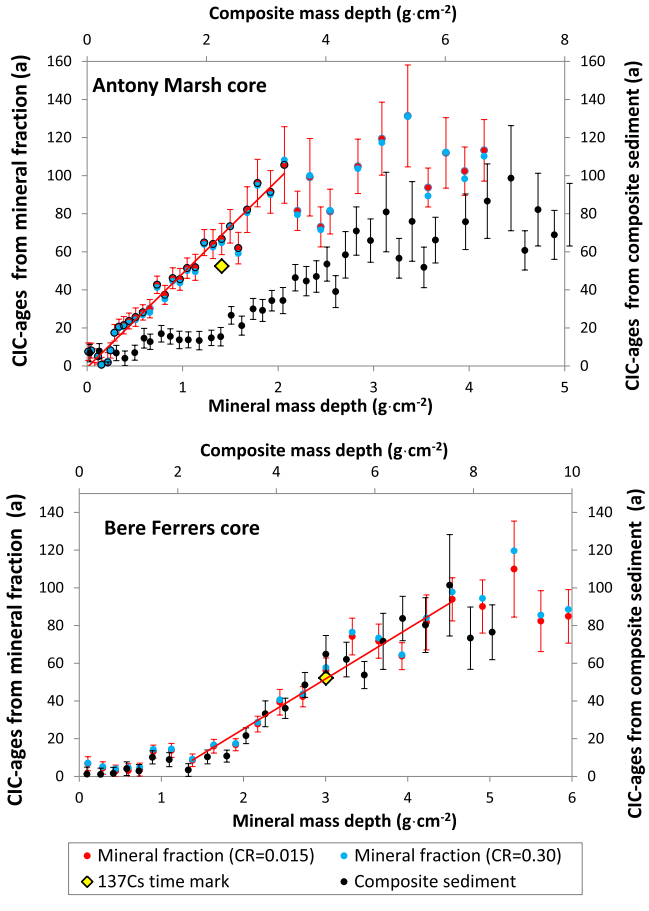

Fig. 9. CIC model applied to the mineral fraction (estimated with two *CR* values) in the two studied sediment cores. Its use with the composite sediment is shown for comparison. The ^{137}Cs time-mark is also depicted (diamond dot) in the mineral mass depth scale. The estimation of model parameters is summarized in Table 3. Linear trends correspond to sedimentary conditions where SARs fluctuate around a constant mean value.

of the initial activity concentration. This value is moderately constrained by a trend-line of ages converging to zero at the SWI (Table 3 summarizes the selected values). The assumption of a constant initial activity concentration leads to the logical trend of increasing ages with depth in the intermediate portion of the cores, but it fails in their upper and lower sections, revealing changes in sedimentological conditions.

Those transects in Fig. 9 with a linear trend of increase in ages correspond to SARs fluctuations around a constant mean value, as it is the case for the mineral fraction in the Antony Marsh core (slope 45.7 ± 1.8, $r = 0.977$, $p < 0.001$, n = 32 for both *CR* values, which corresponds to a SAR value of 0.0219 ± 0.0009 g cm^{-2}a^{-1}), and for an intermediate transect in the Bere Ferrers core (slope 26.6 ± 1.9, $r = 0.975$, $p < 0.001$, n = 12 for both *CR* values, which corresponds to a SAR value of 0.0376 ± 0.0027 g cm^{-2}a^{-1}). Curvilinear trends define varying SARs, as it could be inferred from the composite sediment in the Antony Marsh core. These varying composite SARs are mediated by the decoupled chronological behaviour of the OM.

According to the results above, the use of the CIC model in saltmarshes sediments with high OM content is only physically meaningful when applied to the mineral fraction and using the mineral mass depth scale. For the two studied cores the CIC model is not a good model choice for describing the entire sediment sequence, suggesting changes in sedimentary conditions in the older and younger portions of the cores.

3.4.4. *TERESA model applied to vegetated saltmarshes sediments*

Results from TERESA model are summarized in Figs. 10 and 11, for the Antony Marsh and the Bere Ferrers cores, respectively, including sensitivity tests to *CR* for the former. The fitted model parameters appear in Table 4. These sets of parameter values define the normal distributions which characterize the variability of SARs and initial activity concentrations for the different core sections. The best arrangement (sorting) of these pairs of data allows the estimation of ^{210}Pb$_{exc}$ versus mineral mass depth profile at the time of sampling which best fits the empirical profiles (first panels in Figs. 10 and 11 plotted versus depth, cm).

Once the sorting of the (mineral) SAR values is known, and as the mineral mass thickness of each sediment slice is also known, it is possible to estimate the time interval required for its formation. From this information, a chronology can be built. The propagated uncertainties represent the combined uncertainties associated to each parameter value (Table 4), and they have been estimated following the method presented in Abril (2016) (Figs. 10 and 11, second panels). It is worth noting that unlike in the CRS model, the propagated uncertainties in TERESA model do not necessarily increase with depth, and they can be larger at intermediate portions of the core depending on how the structure of the ^{210}Pb$_{exc}$ profile affects the sorting algorithm.

TERESA does not need the total inventory but it requires the continuity of the sequence. Interpolations can be applied for non-measured slices, but this is not the present case. Nevertheless, ^{210}Pb$_{exc}$ activity concentration had an unreliable value (combined uncertainties higher than 50%) in the slice at 35 cm depth in the Antony Marsh core. This is challenging for the approach of Gaussian distributions, and the model fit to the data below this depth is poor (Fig. 10, first panel, $CR = 1.5 \times 10^{-2}$, n = 42). Thus, the chronology for this transect must be handled with caution. For the present goals, a Multimodal-TERESA approach (Abril, 2020) is not justified. Two additional applications of TERESA to this core account for the ^{210}Pb$_{exc}$ concentrations in the mineral fraction (with the two extreme *CR* values) in the 0–34 cm depth range. They produce good fits to the ^{210}Pb$_{exc}$ profiles (Table 4) and very close chronologies (Fig. 10). The major effect of the *CR* value is the scaling of $\overline{A}_0$ (Table 4), but the main features in the temporal variability of the initial activity concentrations are well replicated by the three runs of the model (Fig. 10, second panel, secondary axis).

In the light of these sensitivity tests for the Antony Marsh core, the application of TERESA to the Bere Ferrers core has been limited to a

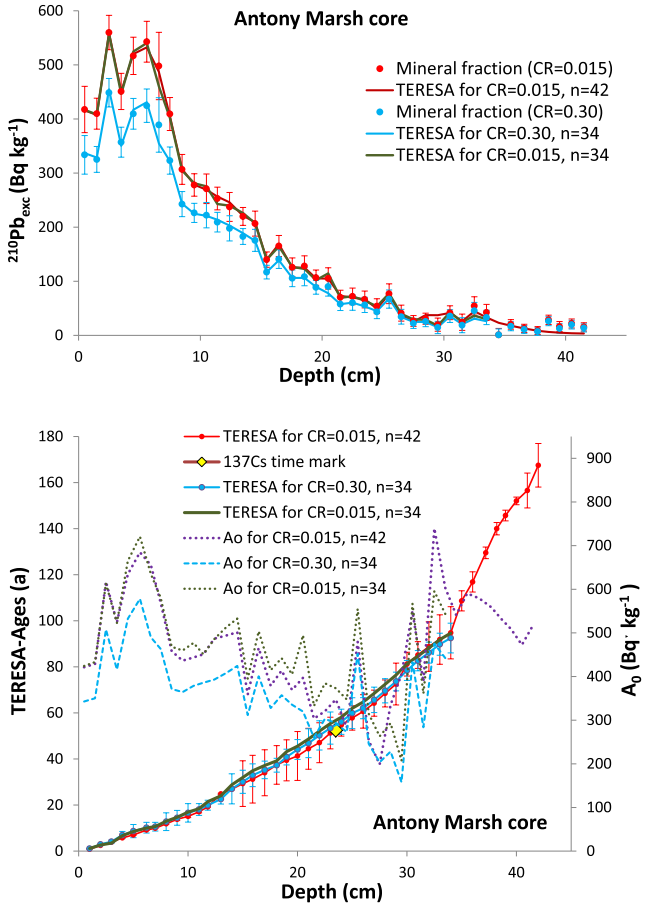

Fig. 10. First panel: $^{210}Pb_{exc}$ activity concentrations in the mineral fraction versus depth in the Antony Marsh sediment core, as estimated by Eq. (12) for two extreme *CR* values (see Table 4). Continuous lines correspond to the best fit provided by TERESA model with the set of parameter values shown in Table 4 (model estimates are plotted at the central point of each sediment slice, and then connected by the continuous line). For $CR = 1.5 \times 10^{-2}$ TERESA has been run in the range of depths from 0 to 42 cm (n = 42) and from 0 to 34 cm (n = 34). Second panel: The ages estimated by the above three runs, according to Table 4 (error bars have been omitted for $CR = 1.5 \times 10^{-2}$, n = 34) along with the ^{137}Cs time mark are shown, while the estimated initial activity concentrations for each slice is plotted in the secondary vertical axis.

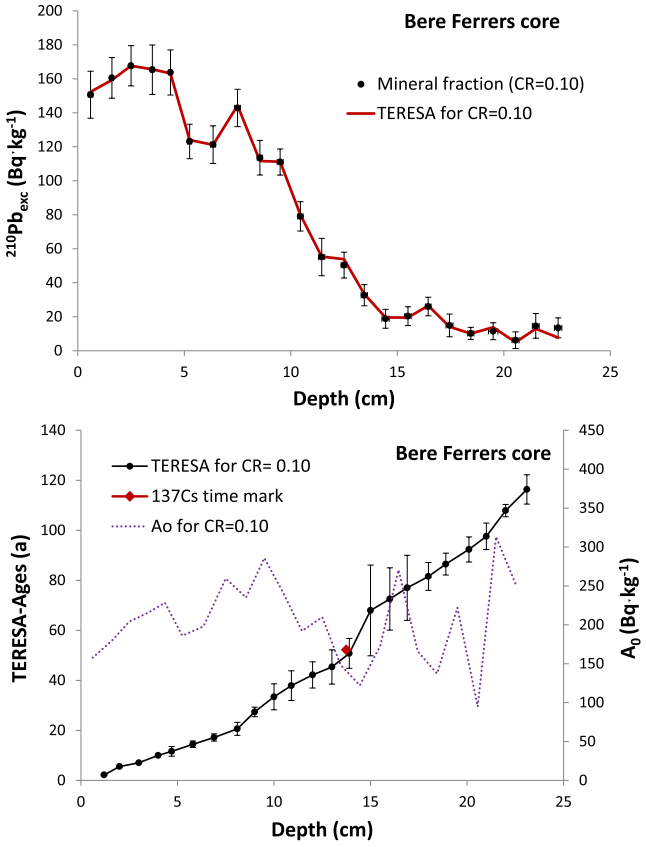

Fig. 11. First panel: $^{210}Pb_{exc}$ activity concentrations in the mineral fraction versus depth in the Bere Ferrers sediment core, as estimated by Eq. (12) for a single *CR* value ($CR = 1.0 \times 10^{-1}$). Continuous lines correspond to the best fit provided by TERESA model with the set of parameter values shown in Table 4. Second panel: The TERESA estimated ages (using $CR = 1.0 \times 10^{-1}$) along with the ^{137}Cs time mark are shown, while the estimated initial activity concentrations for each slice is plotted in the secondary vertical axis.

single intermediate value of *CR* (Fig. 11).

TERESA ages (stand-alone model) are in good agreement with the ^{137}Cs time mark (see second panels in Figs. 10 and 11), which provides an independent validation of the chronology (for the age of 1963).

3.4.5. *Summary: model inter-comparison and linear accretion rates*

Fig. 12 presents a comparison among the chronologies produced by different models for the two studied cores. The CIC model has been omitted for better clarity in the figures.

The use of all radiometric models is limited by the accomplishment of their respective model assumptions.

The CRS and PLUM models work with $^{210}Pb_{exc}$ inventories instead of concentrations, so they can be applied to the composite sediment without need of any further adaption when assuming that $CR \times f_{org} \ll 1$, which seems quite reasonable for the studied cores. The performance of the CRS model is not significant for the Bere Ferrers core because the rate of supply changed over time (as inferred from the reference date method). This also affects the application of PLUM. For Antony Marsh, older dates may be underestimated by the CRS model likely due to the absence of a steady state total inventory.

The other models, which work with activity concentrations, can only be consistently applied to the mineral fraction because the noticeable dilution effect produced by the high OM content of these vegetated coastal sediments (see Fig. 6). Sensitivity tests (Tables 2–4) have shown that the chronology is not significantly affected by an accurate estimation of the parameter *CR*, although a site and plant specific value is always advisable.

The CS model built from the ^{137}Cs time mark lacks any independent validation with the present dataset, particularly for the portion of the core below the peak, but it can provide a valuable first level of understanding. The agreement between the CS model and the ^{137}Cs time mark is not an external validation but a necessary consequence of the particular model construction.

Table 3
Initial activity concentrations (A_0) used for the CIC model and the estimated ages for the sediment slice containing the ^{137}Cs peak in the Antony Marsh and the Bere Ferrers cores.

Sediment fraction	Antony Marsh			Bere Ferrers		
Composite: A_0 (Bq/kg)	145			108		
Composite: Age for ^{137}Cs peak (a)	47	±	8	48	±	7
Mineral ($CR = 0.30$): A_0 (Bq/kg)	420			175		
Mineral ($CR = 0.30$): Age for ^{137}Cs peak (a)	65	±	9	58	±	7
Mineral ($CR = 0.015$): A_0 (Bq/kg)	528			190		
Mineral ($CR = 0.015$): Age for ^{137}Cs peak (a)	63	±	8	56	±	6

For estimating error propagation a 10% of relative uncertainty has been ascribed to A_0. Accounting for the sampling date, the age of the ^{137}Cs peak is 52.2 a.

Table 4

Entry parameters for TERESA model and fitting-error estimates[a], where $\overline{A_0}$ and $\overline{w}$ are the arithmetic mean values of the initial concentration and SAR, respectively, and sA, sw are the corresponding relative standard deviations.

CR	$\overline{A_0}$ (Bq kg^{-1})			$\overline{w}$ (g cm^{-2}a^{-1})			s_A			s_w			χ
	Antony Marsh sediment core												
a	469.0	±	0.6	0.0280	±	0.0003	0.255	±	0.003	0.280	±	0.003	0.69
b	464.0	±	1.0	0.0280	±	0.0002	0.254	±	0.005	0.280	±	0.003	0.33
c	368.0	±	0.4	0.0285	±	0.0009	0.262	±	0.002	0.260	±	0.016	0.31
	Bere Ferrers sediment core												
d	204.0	±	0.6	0.0630	±	0.0006	0.265	±	0.005	0.335	±	0.0041	0.29

[a] Through the second derivative of the Q^2 function (Bevington and Robinson, 2003).*CR* values: a) $CR = 1.5 \times 10^{-2}$, n = 42; b) $CR = 1.5 \times 10^{-2}$, n = 34; c) $CR = 3.0 \times 10^{-1}$, n = 34; d) $CR = 1.0 \times 10^{-1}$, n = 23 (n is the number of data used in the fit).

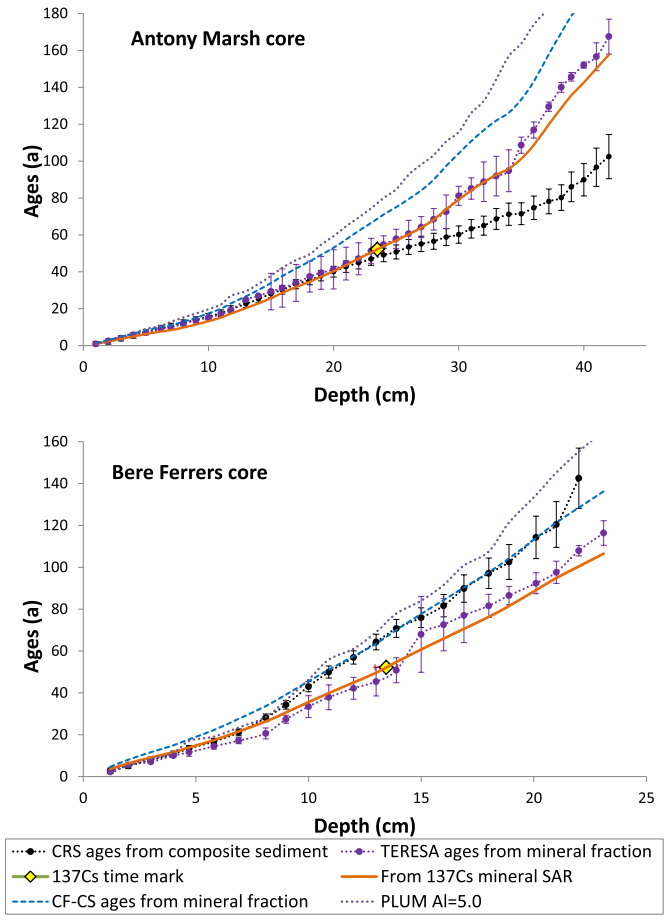

Fig. 12. Chronologies produced for the two studied cores by the models: i) CRS applied to the composite sediment; ii) TERESA applied to the mineral fraction ($CR = 1.5 \times 10^{-2}$for Antony Marsh and $CR = 1.0 \times 10^{-1}$for Bere Ferrers, after the sensitivity tests shown in Fig. 10); iii) CS with the mean mineral SAR estimated from the position of the 1963 peak for ^{137}Cs (Table 2); iv) CF-CS applied to the mineral fraction with $CR = 1.5 \times 10^{-2}$ (Table 2); v) PLUM applied to the composite sediment (only the mean value is shown, see Fig. S4, in ESM, for more details). The ^{137}Cs time mark is shown for comparison.

In the studied cores the CF-CS and CIC models could not satisfactorily explain the structure of the $^{210}Pb_{exc}$ profiles in their upper and deeper portions, most likely due to the temporal variations of both SAR and initial activity concentrations. The performance of TERESA model seems quite reasonable for these cores.

In all cases, the independent validation of the chronologies is limited to a single time mark from the ^{137}Cs peak. It is worth noting that in these cores the first appearance of ^{137}Cs in the atmosphere cannot be used as a time mark because the non-ideal deposition of its fresh fallout, as discussed above (see Fig. 4). Particularly, in both cores, ^{137}Cs has been measured close to the $^{210}Pb_{exc}$ equilibrium depth (see Figs. 4 and 6).

A chronology associates an age to each sediment horizon, and this can be positioned in the core by using linear depth (at the time of the extrusion), composite mass depth or mineral mass depth (see Tables S1 and S2 in ESM). In section 2.5.1 the physical meaning of the mineral sediment accumulation rates have been discussed, while the composite and linear SARs reflect transient stages that change with the below-ground production and decay of OM, its decoupled advective flow, and self-compaction.

According to the TERESA model, the mean values of the mineral SARs are 0.028 g cm^{-2} a^{-1} and 0.0603 g cm^{-2} a^{-1} for the Antony Marsh and the Bere Ferrers cores, respectively (Table 4). The plots of bulk density vs depth (Fig. 3) do not allow identifying an early compaction limit (i.e., a virtually constant value) as the end-point conditions for the current vegetated saltmarsh sediments. The value of mineral bulk density at the deepest slice of the cores (~0.20 g cm^{-3} and ~0.38 g cm^{-3} for Antony Marsh and Bere Ferrers cores, respectively – see Tables S1 and S2, in ESM) can be seen as a lower bound for $\rho_{b,min,ECL}$ (Eq. (10)). From the above figures for mean mineral SARs and Eq. (10) it is possible to estimate an upper bound for the linear accretion velocity of the SWI: $v <$ 1.4 mm a^{-1} for the Antony Marsh core and $v <$ 1.6 mm a^{-1} for the Bere Ferrers core.

4. Conclusions

The ^{210}Pb and ^{137}Cs-based radiometric dating methods provide an insight, at a centennial scale, on the rates of sediment accretion in vegetated saltmarsh sediments. Existing methods require adaptation to these scenarios where below ground production and decay of organic matter introduces a source of achronicity. This paper discusses the applicability of the existing ^{210}Pb radiometric methods and it proposes a reliable tuning, illustrated with the study-cases of the Antony Marsh and Bere Ferrers sediment cores. Major conclusions are:

i) Unsaturated conditions can occur in saltmarsh sediments. Sediment bulk densities should be estimated by direct measurements of dry mass and bulk volume, and they must be corrected for the precipitated salts within the pore fluid.
ii) Due to the achronicity of the OM, the apparent organic component of SAR only reflects transient stages, decoupled from the OM-flows into the SWI. For estimating linear accretion velocities at the SWI (important for sea level rise research), the equations for early compaction limit should be used.
iii) Radionuclides involved in radiometric dating, such as ^{210}Pb, ^{226}Ra, ^{137}Cs and ^{241}Am, are mostly bound to the mineral fraction of the sediments (see Table 1). The high and depth-dependent content of OM in saltmarsh sediments produces a dilution of activity concentrations when referred to the composite matrix.
iv) The CRS and PLUM models work with $^{210}Pb_{exc}$ inventories, not activity concentrations, so they can be applied to the composite sediment when $CR \times f_{org} \ll 1$.

v) ^{210}Pb dating models working with activity concentrations (see Annex A), can only be consistently applied to the mineral fraction of the sediment, when used in coastal or terrestrial systems with high OM content.
vi) Sensitivity tests (Tables 2–4) have shown that ^{210}Pb chronologies are less influenced by an accurate estimation of sediment-to-plant concentration ratio parameter, although a site and plant specific value is always advisable.
vii) The use of each model is limited by the accomplishment of its assumptions in the particular studied sedimentary system.

Declaration of competing interest

The authors declare no conflicts of interest.

Acknowledgments

A.R. Iurian acknowledges the support of a Marie Curie Fellowship (H2020-MSCA–IF–2014, Grant Agreement number: 658863) within the Horizon 2020 during the period 2015–2017. We are grateful to local landowner for access to the field site. William Marshal and Rupert Goddard kindly assisted with collection of sediment cores, Alex Taylor supported the LOI and XRF measurements, Alan D. Tappin supported the analysis of organic carbon and Jamie Quinn the map with the location of saltmarshes.

Annex A. ^{210}Pb-based radiometric dating models for recent sediments

The study of ^{210}Pb found in excess (^{210}Pb$_{exc}$ hereafter) with respect to its parent radionuclide (^{226}Ra) in sediment cores has shown to provide useful insights on the history of the sedimentary systems at a centennial time scale (Mabit et al., 2014).

The ^{222}Rn exhaled from the earth's surface into the atmosphere is rapidly dispersed and it decays to ^{210}Pb, which is removed by precipitation and dry deposition. This fallout ^{210}Pb can reach the surficial sediments where it meets the ^{210}Pb produced by the in situ decay of ^{222}Rn (assumed in secular equilibrium with ^{226}Ra). ^{210}Pb is strongly bound to the solid phase of sediments and it decays with a known half-life (22.3 a).

Although the physical fundamentals for the mass-conservation of a particle-bound radioactive tracer in porous and accreting sediments are relatively well understood (see the revisited diagenetic equations in Abril, 2003), a^{210}Pb$_{exc}$ vs mass depth profile, $A(m)$, by itself, is unable to provide any chronological information without the introduction of a series of assumptions. Any set of assumptions which enables the construction of a chronology from $A(m)$ is known as a radiometric dating model.

It is worth noting that due to self-compaction and to the shortening during coring, storage and extrusion operations, a true depth scale is not physically meaningful. The mass depth scale, m, (dry mass per unit area accumulated from the SWI) remains invariant under the above processes, and it is the one adopted in this work. Mass sedimentation rates will be denoted as SAR, and represented with the symbol w.

A summary of the most known ^{210}Pb-based dating models can be found in Arias-Ortiz et al. (2018). As a brief update of the above review, it is worth mentioning the critical revision of the physical fundamentals of the SIT model (Abril, 2015), the Bayesian formulation of the "constant flux" model, by Aquino-López et al. (2018), known as PLUM model, the multimodal version of TERESA model (Abril, 2020), and the *serac* software package by Bruel and Sabatier (2020).

All the models and the proper diagenetic equations (Abril, 2003) share the fundamental assumption of that the sediment can be treated as a continuous medium, which is characterized by two phases: solids and pore water. The radionuclides of interest are assumed to be particle bound, so, they are virtually absent from the pore water. In what follows, the different models will be presented and discussed under this assumption. Non-ideal deposition will be also discussed. It arises from the failure of the above fundamental hypothesis in some scenarios where inputs of dissolved radio-nuclides (or attached to colloids) can penetrate large depths into sediments with high porosity before being irreversibly bound to the solid phase. The need of adapting these models to the particular conditions of vegetated coastal sediments also focuses on the failure of the assumption of a continuous media. In this case, the failure is related to the achronological character of the belowground production of organic matter, its decay, and its distinct advection processes. The suggested adaptions are presented within the main body of the paper.

Most of the models share three assumptions: i) continuity of the sequence (i.e., there is not any missing layer by erosion, neither major episodic depositional-events); ii) ^{210}Pb$_{exc}$ behaves as a particle-associated tracer and new inputs are ideally deposited at the sediment-water interface (SWI) over the previously existing material; iii) there is no post-depositional redistribution. In reality, they can be broken in some particular sedimentary scenarios and additional models accounting for diffusion, mixing, non-ideal deposition and methods for handling episodic depositional or erosional events are involved. However, even when accomplished, the above three assumptions are still unable to construct a chronology. Effectively, without any additional restrictive assumption, it can be shown that there are an infinite number of possible chronological lines being all of them mathe-matically exact solutions for any given $A(m)$ dataset (see a more detailed discussion in Abril, 2015 and Abril 2019).

Examples of additional assumptions enabling unique solutions are: a) ^{210}Pb$_{exc}$ fluxes onto the SWI, φ , are constant over time (PLUM model by Aquino-López et al., 2018; and CRS model when also assuming steady state inventories - see Appleby and Oldfield, 1978); b) initial activity concentrations, A_0, are constant over time (CIC model; Goldberg, 1963); c) fluxes onto the SWI and SAR are both constant over time (CF-CS model; Robbins, 1978); d) fluxes and SARs can independently vary over time, but imposing a particular (and non-physically justified) choice for a Fourier series expansion (SIT model; Carroll and Lerche, 2003; Abril, 2015); e) varying ^{210}Pb$_{exc}$ fluxes and SARs, but attaining a positive statistical correlation, as shown by Abril and Brunskil (2014) (TERESA model; Abril, 2016; 2020); f) constant SAR (Sánchez-Cabeza and Ruíz-Fernández, 2012). It is worth noting that the above unique solutions become a restricted set of solutions when accounting for the analytical and propagated uncertainties.

CRS model

The CRS model adopts the above assumptions i) to iii), and it assumes a constant rate of supply (a constant ^{210}Pb$_{exc}$ flux onto the SWI) and a steady state for the total inventories. It works with the ^{210}Pb$_{exc}$ inventory below the sediment horizon at mass depth m, Σ_m:

$$\Sigma_m = \int_m^{\infty} A(m')dm' \tag{A-1}$$

The total inventory below the SWI, Σ_0, is given by Eq. A-1 for $m = 0$. Assuming a steady state inventory and a closed system, the age of the sediment horizon at mass depth m is (Appleby and Oldfield, 1978):

$$t_m = \frac{1}{\lambda}\ln\left(\frac{\Sigma_0}{\Sigma_m}\right) \tag{A-2}$$

CIC-model

The CIC model adopts the above assumptions i) to iii), and it assumes a constant initial activity concentration at the SWI, A_0. Then, the age of the sediment horizon at mass depth m, with a measured specific activity concentration $A(m)$, is:

$$t_m = \frac{1}{\lambda}\ln\left[\frac{A_0}{A(m)}\right] \tag{A-3}$$

CF-CS model

The CF–CS model adopts the above assumptions i) to iii), and it assumes a constant $^{210}Pb_{exc}$ flux onto the SWI, φ, and a constant SAR, w. Then, the age of the sediment horizon at mass depth m is $t_m = m/w$. The above assumptions imply a constant initial activity concentration $A_0 = \varphi/w$. Downcore this initial activity concentration only decreases with radioactive decay, and thus, for the sediment horizon at mass depth m:

$$A(m) = A_0 e^{-\frac{\lambda}{w}m} \tag{A-4}$$

The exponential fit of the $^{210}Pb_{exc}$ vs mass depth profile to Eq. A-4 allows estimating the sedimentation rate, and then solving the chronology from the mass depth scale.

SIT model

It is claimed that the SIT model (sediment isotope tomography; Carroll and Lerche, 2003) can handle fluxes and SARs independently varying with time, under the assumptions i) to iii). Nevertheless, it has been shown that this model lacks a sound physical basis; and, particularly, it misuses the Fourier expansion series (Abril, 2015). Consequently, it will not be considered here.

TERESA model

The fundamentals of TERESA (Time Estimates from Random Entries of Sediments and Activities) model and its validation against synthetic cores and real data from varved sediments can be found in the work of Abril (2016) and a multimodal version is presented in Abril (2020). Further applications can be found in Botwe et al. (2017) and Klubi et al. (2017) for harbour and estuarine sediments; thus, only a brief summary is presented in what follows.

The model adopts the above assumptions i) to iii), and it assumes that $^{210}Pb_{exc}$ fluxes are governed by 'horizontal inputs', and thus there is a statistical correlation between fluxes and SAR (Abril and Brunskil, 2014).

For a sediment core which has been sectioned into N slices of mass thickness Δm_i, (i = 1, 2, … N), each one has an associated age interval, ΔT_i, a mean SAR value w_i, and an associated initial activity concentration $A_{0,i}$ (the one encountered for the sediment slice at the SWI). The TERESA model operates with SARs and initial activities for which slice i adopts the values (w_i, $A_{0,i}$), both varying along the core, but closely following normal distributions around their respective arithmetic mean values, $\overline{w}$ and $\overline{A}_0$, with standard deviations σ_w and σ_A, respectively, being s_w and s_A their normalized values (standard deviations divided by the mean values). Provided a first estimation of $\overline{w}$, $\overline{A}_0$, σ_w and σ_A, the model generates independent random distributions for w_i and $A_{0,i}$. Furthermore, an algorithm solves their best arrangement downcore to fit the experimental $^{210}Pb_{exc}$ vs mass depth profile, generating then solutions for the chronological line and for the histories of SAR and fluxes (Abril, 2016). As the result depends on the first estimation of $\overline{w}$, $\overline{A}_0$, σ_w and σ_A, the model applies a mapping technique by iterating the whole process for each parameter varying over a wide range. The error function, Q^2, measures the overall quality of the fit for each individual run of the model:

$$Q^2 = \sum_{i=1}^{N} \frac{\left(A_{th,i} - A_i\right)^2}{\sigma_i^2} \; ; \; \chi^2 = Q^2/f \tag{A-5}$$

where A_i and σ_i are, respectively, the measured value and the analytical error of the activity concentration of the slice with index i; $A_{th,i}$ is the corresponding value estimated by the model, and f is the number of degrees of freedom. Parametric maps of the χ-function serve to find out the best solution and to support error estimates (Abril, 2016; Bevington and Robinson, 2003). Alternatively, the model's output can be better constrained through the use of time markers, when available. In this work, the stand-alone version of the model with the sorting Method A (Abril, 2016) have been applied.

It is worth noting that TERESA does not need the total $^{210}Pb_{exc}$ inventory, but activity measurements must be continuous over the sequence of sediment slices.

CS - constant SAR model

Under assumptions i) to iii) with a constant SAR, w, and varying fluxes, time markers (such as ^{137}Cs peaks) can be used for estimating SAR and then for building up a chronology: $t_m = m/w$. This model can also be used for estimating $A(m)$ profiles from known time series of fluxes at the SWI. Further below it will be discussed its use in combination with models accounting for pre-depositional processes such as the STA model.

PLUM model

The PLUM model is the Bayesian formulation of the "constant flux" model. It was first presented by Aquino-López et al. (2018), with additional developments in the work by Aquino-López et al. (2020). It has the capability of combining in a single software tool the ^{210}Pb and ^{14}C dating methods, but here only the former is discussed. The version of the software for Python (https://github.com/maquinolopez/PyPlum) has been the one used here.

The model implicitly adopts assumptions i) to iii) and considers that $^{210}Pb_{exc}$ fluxes are constant over time, but it does not requires a steady state total inventory, because of what it can be applied to cores with incomplete recovery of inventories. It works with the total ^{210}Pb activity concentration, and the supported fraction can be introduced as input data or estimated from the equilibrium depth. The basic equation for the model establishes that the $^{210}Pb_{exc}$ per unit area contained in a sediment slice is the result of the integrated deposition of the constant flux over a certain time interval, after accounting for radioactive decay. Authors used the Bacon age depth function involving accretion and memory parameters. The model uses prior distributions defining a range of values for $^{210}Pb_{exc}$ fluxes, the supported ^{210}Pb fraction, and the memory and accretion parameters. Then PLUM obtains Monte Carlo samples using the t-walk algorithm (Aquino-López et al., 2018). The model output is a cloud of chronological lines from which the values for the median and the 95% confidence interval can be reported.

The CRS model is the natural limit of the PLUM when the constant flux has lasted for long enough as to achieve a steady state total inventory. Thus, the use of the PLUM model has been demonstrated against the classical CRS solution for real cases and with synthetic cores generated under the assumption of a constant rate of supply (Aquino-López et al., 2018).

Serac software package

Bruel and Sabatier (2020) presented a R-based software package, *serac*, which allows the application of several $^{210}Pb_{ex}$-based dating models, namely CRS, CIC and CFCS models, including their piecewise versions. The software involves nice graphical capabilities for merging different plots, including the depth profiles for ^{137}Cs and/or ^{241}Am for using their associated chronostratigraphic marks, and allows handling instantaneous sedimentary deposits. This software tool could be likely found of interest for a good number of researchers after getting familiar with the R-environment, but the software itself does not contains new model improvements.

Diffusion and mixing

Diffusion of particle-bound radionuclides requires a physical reworking of the sediment with a net null flow of mass. This requires forcing agents, or mechanisms, responsible for such reworking (e.g. bioturbation or tidally-induced erosion and deposition). As far as is known, these forcing mechanisms, although possible in particular cases, have not been described as generic conditions in vegetated saltmarsh sediments. Consequently, this revision of radiometric dating models does not include the family of models accounting for diffusion and mixing (e.g., Robbins and Edgington, 1975; Robbins, 1978; Christensen, 1982; Abril et al., 1992; Laissaoui et al., 2008).

Limitations in the application of the ^{210}Pb-based dating models

Each one of the above six model-assumptions [a) to f)] represents a paradigm on the behaviour of $^{210}Pb_{exc}$ fluxes onto the SWI in aquatic sedimentary systems. So, the model choice must be supported by our best understanding on how the flows of matter and $^{210}Pb_{exc}$ behave in each aquatic sedimentary environment of our particular interest.

Based upon a wide and systematic survey on laminated sediments from marine, riverine and lacustrine environments, Abril and Brunskil (2014) found that $^{210}Pb_{exc}$ fluxes onto the SWI largely varied over time, while they were statistically correlated with SAR. It could be thought that the temporal variability of φ, SAR and A_0 (as observed by Abril and Brunskil, 2014) automatically discards the application of the PLUM, CRS, CIC and CF-CS models. Nevertheless, an analysis of the properties of model-errors has shown that the CRS chronologies can be acceptable even for varying rates of supply positively correlated with SAR, when such variations are randomly distributed in time around a mean value (Abril, 2019). This result can be extended to the CF-CS and CIC models (Abril, 2020). This kind of random variability in fluxes is expected to occur in relatively unperturbed and low-energetic aquatic environments, and it would be linked to short-term climatic variability. Thus, the many application cases of these classical models where their chronologies have been validated against independent chronostratigraphic markers are not in contradiction with the empirical evidence of widespread conditions of varying rates of supply.

More challenging are those situations where the temporal variability in fluxes have not a pure random character. When changes in environmental conditions lead to a stepped shift on the mean value of φ, over which a random variability is superposed; the piecewise version of the models CF-CS, CRS, CIC and TERESA has shown good performance (Abril, 2019, 2020). Nevertheless, when changes in environmental conditions lead to a continuous trend of increase/decrease in φ, classical models failed; however the Multimodal TERESA model has shown some promising results (Abril, 2020).

It is worth noting that, in addition to analytical uncertainties and the propagated errors, the partial or null accomplishment of some of the model assumptions leads to additional *model-errors* (i.e., discrepancies among model-predicted and the true values of ages and SARs). While the former are routinely reported, these latest are not a priori quantifiable.

Beyond boundary conditions: non-ideal deposition

Radionuclides can reach the SWI already bound to solid particles of varying sizes which contribute to growth the sediment structure, or a fraction of them can be into dissolved phase or attached to colloids and small size non-structural particles. Their fate can be quite different in sediments with

high porosities in their upper layers. Radionuclides in solution can penetrate large depths into sediments with high porosity before being irreversibly bound to the solid phase (after what the post-depositional redistribution ceases). Due to the involved time scales, it is possible a mathematical treatment which modifies the diagenetic equation with a depth-distributed source term while the boundary condition at the SWI (involving the $^{210}Pb_{exc}$ fluxes) is consistently updated (Abril and Gharbi, 2012). Long penetration tails have often been observed for ^{137}Cs from the Chernobyl accident and shortly after the bomb-fallout peak. The fingerprint of non-ideal deposition in $^{210}Pb_{exc}$ profiles is their flattening at the top sediment and the appearance of sub-surface maxima. For given sediment the extent of the non-ideal deposition effect depends on the physical carriers of the different radionuclides at the SWI. Particularly, it can be different for $^{210}Pb_{exc}$, ^{137}Cs and ^{7}Be. Quite often meteoric ^{7}Be (half-live 53.1 days) is found to penetrate up to few centimetres depth in sediments with high porosities, what has been considered by many authors as an evidence of mixing (e.g. Arias-Ortiz et al., 2018). Nevertheless, Botwe et al. (2017) have shown that this feature can be explained by non-ideal deposition.

STA model for pre-depositional processes affecting man-made radionuclides

The system-time-average (STA) model (Robbins et al., 2000) is an updated and simpler formulation of the already known idea on the integration of atmospheric fluxes prior reaching the SWI (McCall et al., 1984; Abril and García-León, 1994). The fluxes onto the SWI, φ, are expressed as a function of the atmospheric deposition, F_a, involving the radioactive decay constant of the radionuclide, λ_R, and a system's constant, k_r, with physical dimension of T^{-1}:

$$\frac{dF_S}{dt} = k_r F_a - (\lambda_R + k_r)\varphi \tag{A-6}$$

Intuitively, atmospheric fluxes are accumulated (integrated) in the catchment area while they are transferred towards the sediment at a constant rate k_r. For large-surface catchments, fluxes onto the SWI (and the resulting inventories) are larger than the atmospheric deposition (and its integrated value). This anomaly is solved by the STA model which uses a normalization factor, Z_N, defined as the ratio between the inventory and the integrated fluxes onto the SWI (decay-corrected to the date of sampling). The simplest version of the model works with a constant (mean) value of SAR, which can be first estimated from the peak position, and then further refined (the age of the peak is only slightly displaced by the STA model). This allows conversion of the sequence of φ into activity concentrations, generating their profiles versus mass depths. Thus, STA only involves a free parameter, namely k_r, which is selected to get the best agreement between the measured and the modeled profiles. It is worth noting that for radionuclides with a constant atmospheric deposition (as often assumed for $^{210}Pb_{exc}$), the STA model also leads to a constant flux onto the SWI.

Sediments grain size effects in ^{210}Pb-based dating models

He and Walling (1996) conducted experimental studies on the ^{137}Cs and ^{210}Pb uptake by suspended mineral soil particles in spiked aqueous solutions (their experiments 1 and 2). They suggested an empirical relationship between activity concentrations, C, and a power of the specific surface area of the particles, $S_{sp,}$ being this last in the range 0.1–6 m^2/g. Particularly, from their experiment 1, they found for $^{210}Pb_{exc}$ that $C \propto S_{sp}^{0.67}$.

These experiments were later revisited and interpreted in terms of a basic microscopic theory of the distribution, transfer and uptake kinetics of dissolved radionuclides by suspended particulate matter (Abril, 1998a, 1998b).

He and Walling (1996) also reported radionuclide concentrations in different size fractions of catchment soils receiving natural fallout inputs, and in overbank sediment deposits. These results showed radionuclide concentrations increasing with a certain power of S_{sp}, being this last in the range 0.1–3.5 m^2/g. With the approach of particles with spherical shape and uniform density, the above studies accounted for grain sizes roughly below 25 μm.

Clay-normalized ^{210}Pb activity concentrations have been used for establishing geochronologies of flood events in large tropical river systems (Aalto and Nittrouer, 2012). Sun et al. (2018) found a strong positive correlation between the clay component (<4 μm) and $^{210}Pb_{exc}$ in a wide set of sediment cores from the coastal area of the Yangtze River Estuary.

Based upon the above results and other similar studies, some authors have suggested corrections in ^{210}Pb-based dating models to account for changes in granulometry along the sediment core (e.g., Arias-Ortiz et al., 2018). Nevertheless, it hardly can be assumed that the empirical relationships found by He and Walling (1996) - their Eq. (3), in laboratory conditions (spiked solutions), with a particular soil sample, and studied in the range of sizes < 25 μm, also holds for any natural conditions of coastal sediments and for particles sizes ranging from 4 μm up to 2000 μm. Other authors assume that the sand content of a sediment slice is virtually free of $^{210}Pb_{exc}$ and then they report and use mud-normalized concentrations for applying the CF-CS model (e.g., Sanders et al., 2012).

It is worth noting that the above normalization procedures use the information on particles size distributions, but they do not involve the direct measurements of ^{210}Pb in the physically-separated grain-size classes These kind of measurements have been reported among others, by Alonso--Hernández et al. (2006) for coastal sediments in Cienfuegos Bay, and by Mantero et al. (2019) for some estuarine sediments from Spain and Ghana. Their results showed weak or negligible dependence of ^{137}Cs and $^{210}Pb_{exc}$ concentrations with particle grain sizes in the range from 4 μm up to 2000 μm.

Unlike under ideal experimental conditions, the uptake of radionuclides by suspended particulate matter and surficial sediments in real aquatic environments is the aggregate result of a large variability of chemical-physical conditions and a large diversity of contact times. Consequently, the observed increase in activity concentrations with decreasing particle sizes can be only slight or negligible in the some cases (Mantero et al., 2019). This does not discard stronger relationships in other aquatic environments, but decision on corrections of ^{210}Pb dating models by particle sizes should be taken on case by case basis, and using site specific empirical equations for corrections. This was not the approach adopted for the present work, but TERESA model already accounts for independent variability of SARs and initial activity concentrations, being this last contributed by both particle size effects and the varying contributions of mas flows with different provenances.

References

Aalto, R., Nittrouer, C.A., 2012. ^{210}Pb geochronology of flood events in large tropical river systems. Phil. Trans. R. Soc. A 370, 2040–2074.

Abril, J.M., 1998a. Basic microscopic theory of the distribution, transfer and uptake kinetics of dissolved radionuclides by suspended particulate matter. Part I: theory development. J. Environ. Radioact. 41, 307–324.

Abril, J.M., 1998b. Basic microscopic theory of the distribution, transfer and uptake kinetics of dissolved radionuclides by suspended particulate matter. Part II: applications. J. Environ. Radioact. 41, 325–341.
Abril, J.M., 2003. A new theoretical treatment of compaction and the advective-diffusive processes in sediments. A reviewed basis for radiometric dating models. J. Paleolimnol. 30, 363–370.
Abril, J.M., 2011. Could bulk density profiles provide information about recent sedimentation rates? J. Paleolimnol. 46, 173–186.
Abril, J.M., 2015. Why would we use the Sediment Isotope Tomography (SIT) model to establish a ^{210}Pb-based chronology in recent-sediment cores? J. Environ. Radioact. 143, 40–46.
Abril, J.M., 2016. A ^{210}Pb-based chronological model for recent sediments with random entries of mass and activities: model development. J. Environ. Radioact. 151, 64–74.
Abril, J.M., 2019. Radiometric dating of recent sediments: on the performance of ^{210}Pb-based CRS chronologies under varying rates of supply. Quat. Geochronol. 51, 1–14.
Abril, J.M., 2020. Multimodal-TERESA, a 210Pb-based radiometric dating model for recent sediments under largely varying rates of supply. Quat. Geochronol. 55, 101032.
Abril, J.M., Brunskil, G.J., 2014. Evidence that excess ^{210}Pb flux varies with sediment accumulation rate and implications for dating recent sediments. J. Paleolimnol. 52, 121–137.
Abril, J.M., García-León, M., 1994. The integrated atmospheric flux effect in a radiogeochronological model. J. Environ. Radioact. 24, 65–79.
Abril, J.M., Gharbi, F., 2012. Radiometric dating of recent sediments: beyond the boundary conditions. J. Paleolimnol. 48, 449–460.
Abril, J.M., García-León, M., García-Tenorio, R., Sánchez, C.I., El- Daoushy, F., 1992. Dating of marine sediments by an incomplete mixing model. J. Environ. Radioact. 15, 135–151.
Abril, J.M., San Miguel, E.G., Ruiz-Cánovas, C., Casas-Ruiz, M., Bolívar, J.P., 2018. From floodplain to aquatic sediments: radiogeochronological fingerprints in a sediment core from the mining impacted Sancho Reservoir (SW Spain). Sci. Total Environ. 631–632, 866–878.
Allen, J.R.L., 2000. Morphodynamics of holocene salt marshes: a review sketch from the atlantic and southern north sea coast of europe. Quart. Sci. Rev. 19, 1155–1231.
Allen, J.R.L., Pye, K., 1992. Coastal saltmarshes: their nature and importance. In: Allen, J.R.L., Pye, K. (Eds.), Saltmarshes: Morphodynamics, Conservation and Engineering Significance. Cambridge University Press, pp. 1–18.
Alonso-Hernández, C.M., Díaz-Asencio, M., Muñoz-Caravaca, A., Delfanti, R., Papucci, C., Ferretti, O., Crovato, C., 2006. Recent changes in sedimentation regime in Cienfuegos Bay, Cuba, as inferred from ^{210}Pb and ^{137}Cs vertical profiles. Continent. Shelf Res. 26, 153–167.
Appleby, P.G., Oldfield, F., 1978. The calculation of lead-210 dates assuming a constant rate of supply of unsupported ^{210}Pb to the sediment. Catena 5, 1–8.
Aquino-López, M.A., Blaauw, M., Christen, J.A., Sanderson, N.K., 2018. Bayesian analysis of ^{210}Pb dating. J. Agric. Biol. Environ. Stat. 23, 317–333.
Aquino-López, M.A., Ruiz-Fernández, A.C., Blaauw, M., Sanchez-Cabeza, J.A.-., 2020. Comparing classical and Bayesian ^{210}Pb dating models in human-impacted aquatic environments. Quat. Geochronol. 60, 101106.
Arias-Ortiz, A., Masqué, P., Garcia-Orellana, J., Serrano, O., Mazarrasa, I., Marbà, N., Lovelock, C.E., Lavery, P.S., Duarte, C.M., 2018. Reviews and syntheses: ^{210}Pb-derived sediment and carbon accumulation rates in vegetated coastal ecosystems: setting the record straight. Biogeosci. Discuss. https://doi.org/10.5194/bg-2018-78.
Bakker, J.P., Esselink, P., Dijkema, K.S., van Duin, W.E., de Jong, D.J., 2002. Restoration of salt marshes in The Netherlands. Hydrobiol. (Sofia) 478, 29–51.
Barnett, R.L., Newton, T.L., Charman, D.J., Gehrels, W.R., 2017. Salt-marsh testate amoebae as precise and widespread indicators of sea-level change. Earth Sci. Rev. 164, 193–207.
Bellucci, L.G., Frignani, M., Cochran, J.K., Albertazzi, S., Zaggia, L., Cecconi, G., Hopkins, H., 2007. ^{210}Pb and ^{137}Cs as chronometers for salt marsh accretion in the Venice Lagoon and links to flooding frequency and climate change. J. Environ. Radioact. 97, 85–102.
Bevington, P.A., Robinson, D.K., 2003. Data Reduction and Error Analysis for the Physical Sciences, third ed. McGraw-Hill, New York.
Botwe, B.O., Abril, J.M., Schirone, A., Barsanti, M., Delbono, I., Delfanti, R., Nyarko, E., Lens, P.N.L., 2017. Settling fluxes and sediment accumulation rates by the combined use of sediment traps and sediment cores in Tema Harbour (Ghana). Sci. Total Environ. 609, 1114–1125.
Boyd, B.M., Sommerfield, C.K., Elsey-Quirk, T., 2017. Hydrogeomorphic influences on salt marsh sediment accumulation and accretion in two estuaries of the U.S. Mid-Atlantic coast. Mar. Geol. 383, 132–145.
Bruel, R., Sabatier, P., 2020. *serac*: a R package for ShortlivEd RAdionuclide chronology of recent sediment cores. J. Environ. Radioact. 225, 106449. https://doi.org/10.1016/j.jenvrad.2020.106449.
Carroll, J., Lerche, I., 2003. Sedimentary Processes: Quantification Using Radionuclides. Elsevier, Oxford.
Christensen, E.R., 1982. A model for radionuclides in sediments influenced by mixing and compaction. J. Geophys. Res. 87, 566–572.
Crosby, S.C., Sax, D.F., Palmer, M.E., Booth, H.S., Deegan, L.A., Bertness, M.D., Leslie, H. M., 2016. Salt marsh persistence is threatened by predicted sea-level rise. Estuar. Coast Shelf Sci. 181, 93–99.
Cundy, A.B., Croudace, I.W., 1995. Sedimentary and geochemical variations in a salt marsh/mud flat environment from the mesotidal Hamble estuary, southern England. Mar. Chem. 51, 115–132.
Cundy, A.B., Croudace, I.W., 1996. Sediment accretion and recent sea-level rise in the Solent, Southern England: inferences from radiometric and geochemical studies. Estuar. Coast Shelf Sci. 43, 449–467.
Cundy, A.B., Croudace, I.W., 2017. The fate of contaminants and stable Pb isotopes in a changing estuarine environment: 20 years on. Environ. Sci. Technol. 51, 9488–9497.
Dadey, K.A., Janecek, T., Klaus, A., 1992. Dry-bulk density: its use and determination. In: Taylor, B., Fujioka, K., et al. (Eds.), Proceedings of the Ocean Drilling Program, Scientific Results, 126, pp. 551–554.
De Vos, B., Vandecasteele, B., Deckers, J., Muys, B., 2005. Capability of loss-on-ignition as a predictor of total organic carbon in non-calcareous forest soils, commun. Soil Sci. Plan. 36, 2899–2921.
Dines, H.G., 1956. The Metalliferous Mining Region of South-West England, vol. I. Her Majesty's Stationary Office, BGS, London.
England, Natural, 2016. Plymouth Sound and Estuaries SAC/SSSI: 2013 Saltmarsh Condition Assessment Survey Report (Available online). Accessed March 2016. http://publications.naturalengland.org.uk/publication/5738783394234368.
García-Artola, A., Cearreta, A., Irabien, M.J., Leorri, E., Sanchez-Cabeza, J.A., Corbett, D. R., 2016. Agricultural fingerprints in salt-marsh sediments and adaptation to sea-level rise in the eastern Cantabrian coast (N. Spain). Estuar. Coast Shelf Sci. 171, 66–76.
Goldberg, E.D., 1963. Geochronology with Pb-210. Proceedings of a Symposium of Radioactive Dating. International Atomic Energy Agency, Vienna, pp. 121–131.
He, Q., Walling, D., 1996. Interpreting particle size effects in the adsorption of ^{137}Cs and unsupported ^{210}Pb by mineral soils and sediments. J. Environ. Radioact. 30 (2), 117–137.
Hughes, R.G., 2004. Climate change and loss of saltmarshes: consequences for birds. Ibis 146, 21–28.
IAEA, 2010. Handbook of Parameter Values for the Prediction of Radionuclide Transfer in Terrestrial and Freshwater Environments. International Atomic Energy Agency, TRS No. . 472.
Iurian, A.R., Millward, G.E., Sima, O., Taylor, A., Blake, W., 2018. Self-attenuation corrections for Pb-210 in gamma-ray spectrometry using well and coaxial HPGe detectors. Appl. Radiat. Isot. 134, 151–156.
JCGM, 2008. Evaluation of Measurement Data - Guide to the Expression of Uncertainty in Measurement (GUM 1995 with Minor Corrections), vol. 100, 2008. Joint Committee for Guides in Metrology. http://www.bipm.org/utils/common/documents/jcgm/JCGM_100_2008_E.pdf.
Kauffman, J.B., Donato, D.C., 2012. Protocols for the measurement, monitoring and reporting of structure, biomass and carbon stocks in mangrove forests. In: Working Paper, vol. 86. CIFOR, Bogor, Indonesia.
Kennish, M.J., 2001. Coastal salt marsh systems in the U.S.: a review of anthropogenic impacts. J. Coast Res. 17, 731–748.
Kim, G., Hussain, N., Church, T.M., Carey, W.L., 1997. The fallout isotope ^{207}Bi in a Delaware salt marsh: a comparison with ^{210}Pb and ^{137}Cs as a geochronological tool. Sci. Total Environ 196, 31–41.
Kirwan, M.L., Megonigal, J.P., 2013. Tidal wetland stability in the face of human impacts and sea-level rise. Nature 504, 53–60.
Klubi, E., Abril, J.M., Nyarko, E., Laissaoui, A., Benmansour, M., 2017. Radioecological assessment and radiometric dating of sediment cores from dynamic sedimentary systems of Pra and Volta estuaries (Ghana) along the Equatorial Atlantic. J. Environ. Radioact. 178–179, 116–126.
Koide, M., Soutar, A., Goldberg, E.D., 1972. Marine geochronology with ^{210}Pb. Earth Planet Sci. Lett. 14, 442–446.
Kolker, A.S., Goodbred, S.L., Hameed, S., Cochran, J.K., 2009. High-resolution Records of the response of coastal wetland systems to long-term and short-term sea level. Variability. Estuar. Coast. Shelf Sci. 84, 493–508.
Krishnaswamy, S., Lal, D., Martin, J.M., Meybek, M., 1971. Geochronology of lake sediments. Earth Planet Sci. Lett. 11, 407–414.
Kristensen, E., Bouillon, S., Dittmar, T., Marchand, C., 2008. Organic carbon dynamics in mangrove ecosystem. Aquat. Bot. 89, 210–219.
Laissaoui, A., Benmansour, M., Ziad, N., Ibn Majah, M., Abril, J.M., Mulsow, S., 2008. Anthropogenic radionuclides in the water column and a sediment core from the Alboran Sea: application to radiometric dating and reconstruction of historical water column radionuclide concentration. J. Paleolimnol. 40, 823–833.
Leorri, E., Horton, B.P., Cearreta, A., 2008. Development of a foraminifera-based transfer function in the Basque marshes, N. Spain: implications for sea-level studies in the Bay of Biscay. Mar. Geol. 251, 60–74.
Livesley, S.J., Andrusiak, S.M., 2012. Temperate mangrove and salt marsh sediments are a small methane and nitrous oxide source but important carbon store. Estuar. Coast Shelf Sci. 97, 19–27.
Mabit, L., Benmansour, M., Abril, J.M., Walling, D.E., Meusburger, K., Iurian, A.R., Bernard, C., Tarjan, S., Owens, P.N., Blake, W.H., Alewell, C., 2014. Fallout ^{210}Pb as a soil and sediment tracer in catchment sediment budget investigations: a review. Earth Sci. Rev. 138, 335–351.
Madsen, A.T., Murray, A.S., Andersen, T.J., Pejrup, M., 2007. Temporal changes of accretion rates on an estuarine salt marsh during the late Holocene — reflection of local sea level changes? The Wadden Sea, Denmark. Mar. Geol. 242, 221–233.
Mantero, J., Abril-Hernández, J.M., Garcia-Tenorio, R., Klubi, E., Nyarko, E., 2019. Experimental study on the use of granulometric speciation for the radiometric dating of recent sediments. J. Environ. Radioact. 208–209, 106016. https://doi.org/10.1016/j.jenvrad.2019.106016.
Marchand, C., 2017. Soil carbon stocks and burial rates along a mangrove forest chronosequence (French Guiana). For. Ecol. Manag. 384, 92–99.
Marshall, W.A., Gehrels, W.R., Garnett, M.H., Freeman, S.P.H.T., Maden, C., Xu, S., 2007. The use of 'bomb spike' calibration and high-precision AMS ^{14}C analyses to date salt-marsh sediments deposited during the past three centuries. Quat. Res. 68, 325–337.
McCall, P.L., Robbins, J.A., Matisoff, G., 1984. ^{127}Cs and ^{210}Pb transport and geochronologies in urbanized reservoirs with rapidly increasing sedimentation rates. Chem. Geol. 44, 33–65.

Middelburg, J.J., Vlug, T., van der Nat, F.J.W.A., 1993. Organic matter mineralization in marine systems. Global Planet. Change 8, 47–58.
Mighanetara, K., Braungardt, C.B., Rieuwerts, J.S., Azizi, F., 2009. Contaminant fluxes from point and diffuse sources from abandoned mines in the River Tamar catchment, UK. J. Geochem. Explor. 100, 116–124.
Nature, English, 2006 (online). Available from: accessed. www.english-nature.org.uk. (Accessed 14 March 2016).
Nellemann, C., Corcoran, E., Duarte, C.M., Valdes, L., DeYoung, C., Fonseca, L., Grimsditch, G., 2009. Blue carbon. A Rapid Response Assessment. United Nations Environment Programme, GRID-Arendal, Norway.
Pedersen, J.B.T., Bartholdy, J., Christiansen, C., 2007. ^{137}Cs in the Danish Wadden Sea: contrast between tidal flats and salt marshes. J. Environ. Radioact. 97, 42–56.
Ralph, I.S., 1956. The ecology of the Tamar Estuary VII. Observations of the interstitial salinity of intertidal muds in the estuarine habitat of *Nereis Diversicolor*. J. Mar. Biol. Assoc. U. K. 35, 81–104.
Robbins, J.A., 1978. Geochemical and Geophysical applications of radioactive lead isotopes. In: Nriago, J.P. (Ed.), Biochemistry of Lead in the Environment. Elsevier, Amsterdam, pp. 285–393.
Robbins, J.A., Edgington, D.N., 1975. Determination of recent sedimentation rates in Lake Michigan using ^{210}Pb and ^{137}Cs. Geochem. Cosmochim. Acta 39, 285–304.
Robbins, J.A., Holmes, C., Halley, R., Bothner, M., Shinn, E., Graney, J., Keeler, G., ten Brink, M., Orlandini, K.A., Rudnick, D., 2000. Time-averaged fluxes of lead and fallout radionuclides to sediments in Florida Bay. J. Geophys. Res. 105, 28805–28821.
Ruíz-Fernández, A.C., Carnero-Bravo, V., Sanchez-Cabeza, J.A., Pérez-Bernal, L.H., Amaya-Monterrosa, O.A., Bojórquez-Sánchez, S., López-Mendoza, P.G., Cardoso-Mohedano, J.G., Dunbar, R.B., Mucciarone, D.A., Marmolejo-Rodríguez, A.J., 2018. Carbon burial and storage in tropical salt marshes under the influence of sea level rise. Sci. Total Environ. 630, 1628–1640.
Sanchez, A.L., Wright, S.M., Smolders, E., Naylor, C., Stevens, P.A., Kennedy, V.H., Dodd, B.A., Singleton, D.L., Barnett, C.L., 1999. High plant uptake of radiocesium from organic soils due to Cs mobility and low soil K content. Environ. Sci. Technol. 33, 2752–2757.
Sánchez-Cabeza, J.A., Ruíz-Fernández, A.C., 2012. ^{210}Pb sediment radiochronology: an integrated formulation and classification of dating models. Geochem. Cosmochim. Acta 82, 183–200.
Sanders, C.J., Smoak, J.M., Waters, M.N., Sanders, L.M., Brandini, N., Patchineelam, S.R., 2012. Organic matter content and particle size modifications in mangrove sediments as responses to sea level rise. Mar. Environ. Res. 77, 150–155. https://doi.org/10.1016/j.marenvres.2012.02.004.
Sun, X., Fan, D., Tian, Y., Zheng, S., 2018. Normalization of excess 210Pb with grain size in the sediment cores from the Yangtze River Estuary and adjacent areas: implications for sedimentary processes. Holocene 28 (4), 545–557.
Vidmar, T., 2005. Efftran - a Monte Carlo efficiency transfer code for gamma-ray spectrometry. Nucl. Instrum. Methods 550, 603–608.
Wilson, C.A., Hughes, Z.J., FitzGerald, D.M., Hopkinson, C.S., Valentine, V., Kolker, A.S., 2014. Saltmarsh pool and tidal creek morphodynamics: dynamic equilibrium of northern latitude saltmarshes? Geomorphology 213, 99–115.
Wright, S.M., 2016. Predicted Caesium-137 Deposition from Atmospheric Nuclear Weapons Tests. NERC Environmental Information Data Centre. https://doi.org/10.5285/c3e530bf-af20-43fc-8b4b-92682233ff08.
Yang, J., Gao, J., Liu, B., Zhang, W., 2014. Sediment deposits and organic carbon sequestration along mangrove coasts of the Leizhou Peninsula, southern China. Estuar. Coast Shelf Sci. 136, 3–10.